

POLITECNICO DI MILANO
School of Industrial and Information Engineering
Department of Physics
Master of Science Thesis Work



**Application of Scaled Wave Optics Propagator to
Model Synchrotron Beamlines**

Supervisor:

Prof. Giacomo Claudio Ghiringhelli

Assistant Supervisor:

Dr. Manuel Sanchez del Rio

Candidate:

Giovanni Pirro

Academic Year 2016-2017



The whole work presented in these pages was carried out at the European Synchrotron Radiation Facility (ESRF), in Grenoble, under the supervision of dr. M. Sanchez del Rio.

Acknowledgments

I am deeply grateful to Manuel Sanchez del Rio for being the most propoitive and supporting supervisor one can ever hope to have.

I would like to thank Jason Schmidt for his help in pointing me in the right direction when working on this project and David Paganin for giving me his time for endless and fruitful discussions.

I would like to thank Rafael Celestre for always being available for confrontations and all the people and friends I have met in Grenoble. Among them a special thank goes to Caterina for being a very nice flat mate.

My deepest gratitude goes to Beatrice that has always encouraged me and has always been there for me, and to my parents and my sister for their constant support.

Finally, I would like to show my gratitude to professor Giacomo Ghiringhelli for making this experience possible.

Contents

1 Acknowledgment	5
Prefazione	i
Abstract	iii
2 Introduction	1
3 Theory of X-Ray wave optics	5
3.1 Introduction to linear systems	5
3.2 Introduction to Fourier analysis	8
3.3 From Fourier transform to discrete Fourier transform	12
3.4 Scalar electromagnetic theory	17
3.5 Scalar diffraction theory	20
3.5.1 Angular spectrum method	21
4 Wavefront propagator and implementations	25
4.1 Introduction of a magnification factor	28
4.2 Physical interpretation	31
4.3 Validity conditions	35
5 Discussion and applications	39
5.1 Aliasing conditions	40
5.2 The ESRF beamline ID16A	48
5.3 Simulation of the effect of a decoherer system	53
6 Conclusions	57
A The OASYS Graphical Environment	59
Bibliography	62

List of Figures

3.1	Spectrum of the 'chirp' function	12
3.2	Graph of example continuous function $g(x)$ and $G(f_x)$	14
3.3	Aliasing effect due to discretization of $g(x)$	15
3.4	Blurring effect caused by windowing of $g(x)$	15
3.5	Virtual replicas of $g(x)$ due to finite sampling of $G(f_x)$	16
4.1	Fresnel scaling theorem optical system's schematics	31
5.1	FFT example	39
5.2	FFT example for an aliased spectrum	40
5.3	Schematic of the optical system used to prove validity conditions	41
5.4	Comparison between theoretical validity condition of propagation and ex- perimental results	42
5.5	Well propagated wavefronts	44
5.6	Propagation with artifacts	44
5.7	Example of completely wrong propagation	45
5.8	Schematic of the second optical system used to prove validity conditions . .	45
5.9	Comparison between theoretical validity condition of propagation and ex- perimental results and example of well propagated and aliased images . . .	46
5.10	Example of too strict validity conditions	47
5.11	Dependency of the validity conditions on the radius of curvature	47
5.12	Schematics of ID16A	49
5.13	Intensity profiles of ID16A source on plane situated 28.3 m from the center of the undulator	50
5.14	Comparison between the simulation performed with Oasys and with SRW for ID16A (VSS plane)	51

5.15 Comparison between the simulation performed with Oasys and with SRW for ID16A (KBv plane)	51
5.16 Comparison between the simulation performed with Oasys and with SRW for ID16A (sample plane)	52
5.17 Example of validity conditions for the simulation of ID16A	53
5.18 Measured and simulated FWHM without the decoherer	54
5.19 FWHM for Normal random phase screen model	55
A.1 OASYS GUI	60
A.2 OASYS widget GUI	61

Prefazione

Il programma di upgrade dello storage ring di ESRF (EBS) renderà il fascio di raggi X fino a 100 volte più coerente facendo aumentare conseguentemente i fenomeni di interferenza. Questa proprietà è fondamentale per tecniche come l'olografia o l'imaging a contrasto di fase. La caratterizzazione quantitativa della coerenza del fascio permette una migliore progettazione degli esperimenti e l'analisi di dati meno dispendiosa in termini di tempo e risorse. La simulazione al computer delle beamline è lo strumento più efficace per una prima analisi delle caratteristiche del fascio sui vari elementi ottici.

Lo scopo di questo progetto è stato implementare in Python un propagatore con un fattore di scaling da integrare nell'ambiente grafico OASYS per la simulazione ottica di raggi X. Inoltre è stato effettuato uno studio del range dei valori del fattore di magnificazione per ottenere una propagazione senza artefatti. Questo propagatore è il primo passo per la progettazione di una beamline e la caratterizzazione del fascio di raggi X. In particolare, grazie alla futura unione con il pacchetto COMSYL, per la decomposizione in modi coerenti della radiazione di sincrotrone, questo progetto sta alla base di un futuro sviluppo del software per la modellizzazione di un'intera beamline con l'analisi delle caratteristiche della parziale coerenza del fascio e della non idealità degli elementi ottici.

Abstract

The ESRF storage ring upgrade program (EBS) will make the X-ray beam up to 100 times more coherent and consequently increase the interference phenomena. This property is fundamental to techniques such as holography or phase contrast imaging. The quantitative characterization of the coherence allows to optimally design experimental setup and a reduce time and resources necessary for the analysis of data. The beamline computer simulation is the most effective tool for a first analysis of the beam characteristics on the various optical elements.

The aim of this project was to implement in Python a scaled propagator to be integrated into the OASYS graphic environment for optical X-ray simulation and the study of the range of the values of the magnification factor to obtain a propagation without artifacts. This propagator is the first step towards the complete characterization of the X-ray beam and the design of a beamline. In particular, thanks to the future union with the COMSYL package, for the coherent mode decomposition of synchrotron radiation, this project is the basis of a software for the modeling of a whole beamline with the analysis of the characteristics of the partial coherence of the beam and the non-ideality of the optical elements.

Introduction

The calculation of the properties of X-Ray beam and its propagation along a synchrotron beamline is essential for designing, optimizing and operating it. Studying the characteristics of beam coherence and its effect on the optical elements makes it possible to design experimental setup with some required characteristics before actually building it.

When spatial coherence of light is small diffraction effects are negligible and simple, yet, powerful geometric optic theory is functional for the task of simulating the trajectory of the light and the aberrations introduced by the optic elements. However, when coherence becomes a factor (as it will be the case for the new ESRF source (EBS) [1]) the necessity of a more complete and complex theory becomes significant, a theory that models the wavefield as a spatial distribution of complex-valued field amplitude and that can describe the effect of interference.

A full wavefront optics simulation is an iterative process, where the user has to refine the sampling parameters element by element to be sure that the wavefront at each position is sampled correctly. This is a time consuming work to perform with the full 2D simulation. For this reason, a wavefront calculation may be started by a simplified system, using simplified models for the source and focusing elements: the process starts with a first calculation in the approximation of a fully coherent source emitting a wavefront that is propagated through the beamline from element to element (drift spaces) via the integral diffraction formula obtained by the solution of the Helmholtz wave equation that describes the characteristics of a propagating wavefield at a certain position in space. The following step requires to take into account the actual partial coherence of the beam and the non ideality of the optical elements.

The simulations are performed solving the Fresnel-Kirchhoff integral diffraction formula and usually this is done by directly calculating the integral numerically at each pixel of the image plane. This is a costly approach from the computer point of view, and the development of a Fourier Optics theory that uses Fourier transforms helps reduce complexity and

calculation time. This is practically the only choice for simulating 2D images. The use of Fourier Transforms unfortunately adds another problem linked to the discretization process involved in computer computations that makes the result very dependent on the sampling of the wavefront (i.e. pixel size, number of points, dimension of the window where the wavefront is sampled). This matter implies that one has to take some precaution when using these tools. Moreover, classic methods don't make it possible to change the coordinate scale: this means that it is not possible to visualize on the screen a propagated diverging beam unless the initial window size is big enough to contain it all or it is not possible to appreciate the details of the diffraction pattern for a converging beam if the initial sampling grid is not dense enough. For this reason in this work we have studied and developed a propagator based on Fourier optics that makes it possible to vary the pixel size of the object window in order to be able to keep information that would otherwise be lost. Because the horizontal and vertical coupling is usually small in synchrotron beamlines, we have developed a propagator that can act with different scaling parameters on the vertical and horizontal planes. Moreover, we have provided a way to determine the right scaling parameter to completely remove the problems that derive from discretization of the wavefront upfront of its computer simulated propagation.

The propagator has been implemented for the wave optics tool Wofry [2] that is part of the open-source graphical environment for optic simulation OASYS (OrANGE SYnchrotron Suite) [3], [4] developed by Manuel Sanchez del Rio and Luca Rebuffi. This software is already used for simulations of the beam optics for different beamlines. It puts together several packages that allow a user-friendly simulation of the coherent characteristics of photon beams that goes from the ray tracing tool SHADOW [5] to the new module for coherent mode propagation, COMSYL [6]. COMSYL package makes the coherent mode decomposition of synchrotron radiation emitted by electrons passing through an undulator placed in a storage ring and will allow the simulation of the partial coherence that characterizes synchrotron beam.

In this work we have given a proof of the validity conditions found for the correct propagation without artifacts and we have shown two examples of real applications: one is the first step of the simulation of the ESRF beamline ID16A, tested against the well established package

SRW [7], for the study of the future upgrade that will follow to the new ESRF source one. The other one is the study of the effect of a decoherer on the beam, to estimate the best position of this element in the ESRF beamline ID17.

The work is divided in three main parts. The first one serves as a theoretical introduction of those elements needed to develop a scalar diffraction theory through the plane-wave spectral decomposition. The second parts focuses on the development of a propagator that can be easily used for computer simulations and on the introduction of two magnification factors for the vertical and horizontal planes perpendicular to the direction of propagation of the wavefront. Moreover, the condition for a propagation with no artifacts are shown and discussed. The final parts deals with the tests done with this tool and with examples of its use for real studies and simulations and a brief description of the OASYS suite.

Theory of X-Ray wave optics

We are interested in studying phenomena where light coherence is important, such as interference and diffraction. It is appropriate to describe light as a spatial distribution of complex-valued field amplitude developing an electromagnetic wave theory instead of the simpler geometrical optics. As many other physical phenomena, the propagation of light through most media, described by a wave equation, can be seen as a linear mapping of the light electric field distribution at initial and final positions. The property of linearity greatly reduces the effort needed to solve a problem thanks to the simplification of the mathematical description of such phenomena. This means that an electromagnetic disturbance can be decomposed into a linear combination of elementary disturbances and that the result of a propagation can be threatened as the sum of all the source components responses. The advantage is, thus, given by the possibility to express the response to a complicated stimulus in terms of a combination of simpler ones. In this chapter we provide the theoretical basis for developing the angular spectrum method. This method is an alternative way of solving the Helmholtz differential equation, that describes the propagation of a wave, to the most common solution provided by the Kirchhoff diffraction formula. We are interested in its computer implementation that will allow us to make calculations of optical systems such as synchrotron beamlines. We will provide a short introduction on the the theory of linear systems and the Fourier analysis, following the approach of Goodman [8], in order to use it to build a diffraction theory of light.

Introduction to linear systems

We now show that the property of linearity makes it possible to consider the decomposition of a wave-field into a superposition simpler components, namely the the Fourier decomposition. A system is defined to be a mapping of a set of input functions into a set of output functions: for imaging systems, inputs and outputs can be real-valued functions (intensity)

or complex-valued functions (field amplitude) of a two-dimensional variable (space). The assumption of linearity yields to simple mathematical representation of such systems and useful relations between inputs and outputs. The condition for a system to be linear is that the following expression is valid:

$$\mathcal{S}\{ap(x_1, y_1) + bq(x_1, y_1)\} = a\mathcal{S}\{p(x_1, y_1)\} + b\mathcal{S}\{q(x_1, y_1)\} \quad (3.1)$$

where $p(x_1, y_1)$ and $q(x_1, y_1)$ are the input functions, \mathcal{S} is the mathematical operator that identifies a system that act on an input function $g_1(x_1, y_1)$ to return the output function $g_2(x_2, y_2)$:

$$g_2(x_2, y_2) = \mathcal{S}\{g_1(x_1, y_1)\} \quad (3.2)$$

and a and b are two complex constants. As it was said at the beginning of the chapter, the great advantage given by linearity is the possibility to express the output of a system as a combination of the responses of all the elementary components of the input function to the action of the systems. This decomposition is possible because of the so-called shifting property of the δ function which states that:

$$g_1(x_1, y_1) = \int_{-\infty}^{\infty} \int_{-\infty}^{\infty} g_1(\xi, \eta) \delta(x_1 - \xi, y_1 - \eta) d\xi d\eta \quad (3.3)$$

This equation can be interpreted as a linear combination of shifting δ functions weighted by the function g_1 . The output g_2 obtained in response to a stimulus can then be found as:

$$g_2(x_2, y_2) = \mathcal{S}\left\{ \int_{-\infty}^{\infty} \int_{-\infty}^{\infty} g_1(\xi, \eta) \delta(x_1 - \xi, y_1 - \eta) d\xi d\eta \right\} \quad (3.4)$$

and applying the property of linearity (cf. equation 3.1) upon considering the $g_1(\xi, \eta)$ function as simply a weighting factor, the \mathcal{S} operator can be brought into the integral:

$$g_2(x_2, y_2) = \int_{-\infty}^{\infty} \int_{-\infty}^{\infty} g_1(\xi, \eta) \mathcal{S}\{\delta(x_1 - \xi, y_1 - \eta)\} d\xi d\eta \quad (3.5)$$

It is possible to rename the response of a system, for each position (x_2, y_2) of the output space, to a δ function input of the coordinates (ξ, η) of the input space with the symbol $h(x_2, y_2; \xi, \eta)$, such that:

$$h(x_2, y_2; \xi, \eta) = \mathcal{S}\{\delta(x_1 - \xi, y_1 - \eta)\} \quad (3.6)$$

It takes the name of impulse response of the system, and makes it so that the system input and output can be related by the expression:

$$g_2(x_2, y_2) = \int_{-\infty}^{\infty} \int_{-\infty}^{\infty} g_1(x_1, y_1) h(x_2, y_2; \xi, \eta) d\xi d\eta \quad (3.7)$$

This result is fundamental because it is the proof that a linear system is completely characterized by its responses to unit impulses. To completely specify the output, the responses must be known for the impulses located at each of the possible positions of the input plane. Input-output relations for a general linear system can be further simplified for invariant linear systems: a linear imaging system is space-invariant if its impulse response $h(x_2, y_2; \xi, \eta)$ only depends on the distances $(x_2 - \xi)$ and $(y_2 - \eta)$. The response function becomes:

$$h(x_2, y_2; \xi, \eta) = h(x_2 - \xi; y_2 - \eta) \quad (3.8)$$

The superposition integral of equation 3.7 can be now written in the form of a two-dimensional convolution between the input function and the impulse response:

$$g_2(x, y) = \int_{-\infty}^{\infty} \int_{-\infty}^{\infty} g_1(\xi, \eta) h(x - \xi, y - \eta) d\xi d\eta \quad (3.9)$$

This new class of linear systems, namely the invariant linear systems, is described by a very detailed mathematical structure which makes dealing with them a much easier task. This becomes especially clear when noting that by applying the Fourier transform of the two sides of equation 3.9 and invoking the convolution theorem (cf. 3.15):

$$G_2(f_x, f_y) = H(f_x, f_y)G_1(f_x, f_y) \quad (3.10)$$

where $H(f_x, f_y)$, the Fourier transform of $h(\xi, \eta)$, is the transfer function of the system in the Fourier frequency domain:

$$H(f_x, f_y) = \int_{-\infty}^{\infty} \int_{-\infty}^{\infty} h(\xi, \eta) e^{-i2\pi(f_x\xi + f_y\eta)} d\xi d\eta \quad (3.11)$$

This means of finding the output of a system is much more convenient compared with the calculation of a convolution operation. At this point in the discussion, it is worth mentioning that relations 3.10 and 3.11 seems to indicate that, for such class of systems, decomposing the input into elementary functions that are not δ functions but are complex-exponential functions instead, can be more convenient. This decomposition is, of course, done when Fourier transforming $g_1(x_1, y_1)$. The multiplication of the spectrum of g_1 with the transfer function $H(f_x, f_y)$ makes it so every elementary component is affected by the system acting on it. The result is a change in amplitude and a phase shift of these components at each (f_x, f_y) . By inverse Fourier transforming the resulting spectrum of the output function $G_2(f_x, f_y)$ the modified components are added up to return the output $g_2(x_2, y_2)$.

Introduction to Fourier analysis

We give here a short introduction on the Fourier analysis following the work of Goodman [8]. The Fourier transform of a function $f = f(x, y)$ is:

$$G(f_x, f_y) = \mathcal{F}\{g\} = \int_{-\infty}^{\infty} \int_{-\infty}^{\infty} g(x, y) e^{-i2\pi(f_x x + f_y y)} dx dy \quad (3.12)$$

where the transformed function $G = G(f_x, f_y)$ is itself a complex-valued function in the frequency variables (f_x, f_y) . It is possible to also define an inverse Fourier transform of the function G :

$$g(x, y) = \mathcal{F}^{-1}\{G\} = \int_{-\infty}^{\infty} \int_{-\infty}^{\infty} G(f_x, f_y) e^{i2\pi(f_x x + f_y y)} df_x df_y \quad (3.13)$$

one can interpret this expression as a linear superposition of elementary functions of the spatial frequency (f_x, f_y) , $e^{i2\pi(f_x x + f_y y)}$, all weighted by factor $G(f_x, f_y)$. Further discussions on the mathematical concept are left to the interested reader in ref. [9]. The Fourier analysis is an important tool for the study of linear systems because it provides a method to decompose an input into a number of simpler ones. For each of this elementary components the response to a stimulus can be calculated and linearly combined to obtain the output for the initial, more complex, function.

Among all the property of Fourier transform, some in particular are important for the development of this work. The similarity theorem states: if $\mathcal{F}\{g(x, y)\} = G(f_x, f_y)$, then:

$$\mathcal{F}\{g(ax, by)\} = \frac{1}{|ab|} G\left(\frac{f_x}{a}, \frac{f_y}{b}\right) \quad (3.14)$$

A stretch in one space corresponds to a contraction in the conjugate space together with amplitude rescaling. The convolution theorem, already used in equation 3.9, states that, if $\mathcal{F}\{g(x, y)\} = G(f_x, f_y)$ and $\mathcal{F}\{h(x, y)\} = H(f_x, f_y)$, then:

$$\mathcal{F}\{g(x, y) * h(x, y)\} = \mathcal{F}\left\{ \int_{-\infty}^{\infty} \int_{-\infty}^{\infty} g(x', y') h(x - x', y - y') dx' dy' \right\} \quad (3.15)$$

$$= G(f_x, f_y) H(f_x, f_y) \quad (3.16)$$

The convolution in real space, identified by the operator $*$, is equivalent to performing the inverse Fourier transformed product of the two functions' Fourier transform. Each Fourier component of a function is a complex exponential of a unique spatial-frequency, thus it extends over the entire plane (x, y) . For this reason, no univoque relation can be found between a particular spatial coordinate and another spatial frequency. However, in practice, it is possible to relate some region of an image to certain particular frequencies. The concept of local spatial frequency is here introduced and a relation with Fourier components is explained.

We will exploit this concept when dealing with the Nyquist-Shannon sampling theorem in chapter 3.3; in fact, it is essential to estimate the maximal spatial-frequency of a certain field to determine the minimum sample rate that permits a discrete sequence of samples to capture all the information from a continuous-time signal of finite bandwidth. The most general case of complex-valued functions is studied here. Such function can be represented in the form of an amplitude $A(x, y)$ and a phase $e^{i\phi(x, y)}$:

$$g(x, y) = A(x, y)e^{i\phi(x, y)} \quad (3.17)$$

where $A(x, y)$ is a real non-negative amplitude and $\phi(x, y)$ a real phase distribution. In the case in which A is a slowly varying function, the attention can be given to the phase term. Local spatial frequency of the function $g(x, y)$ will be defined as:

$$\begin{cases} f_{lx} = \frac{1}{2\pi} \frac{\partial}{\partial x} \phi(x, y), & \text{if } g(x, y) \neq 0 \\ f_{lx} = 0, & \text{if } g(x, y) = 0 \end{cases} \quad \begin{cases} f_{ly} = \frac{1}{2\pi} \frac{\partial}{\partial y} \phi(x, y), & \text{if } g(x, y) \neq 0 \\ f_{ly} = 0, & \text{if } g(x, y) = 0 \end{cases} \quad (3.18)$$

When applying this result to a Fourier component:

$$g(x, y) = e^{i2\pi(f_x x + f_y y)} \quad (3.19)$$

the local frequency obtained are:

$$f_{lx} = \frac{1}{2\pi} \frac{\partial}{\partial x} [2\pi(f_x x + f_y y)] = f_x \quad f_{ly} = \frac{1}{2\pi} \frac{\partial}{\partial y} [2\pi(f_x x + f_y y)] = f_y \quad (3.20)$$

So in this specific case the local frequency actually correspond to the spatial-frequency of that component. When dealing with a space-limited version of a quadratic-phase exponential function, which will be used later on in the theory of diffraction:

$$g(x, y) = e^{i\alpha(x^2+y^2)} \text{rect}\left(\frac{x}{2L_x}\right) \text{rect}\left(\frac{y}{2L_y}\right) \quad (3.21)$$

the local frequency found can be seen to have a linear dependency on (x, y) position:

$$f_{lx} = \alpha x \text{rect}\left(\frac{x}{2L_x}\right) \quad f_{ly} = \alpha y \text{rect}\left(\frac{y}{2L_y}\right) \quad (3.22)$$

The spatial frequency varies linearly with the position in the plane, within an area determined by the rectangular function $\text{rect}(x)$. It can be shown that the Fourier spectrum of $g(x, y)$ is also approximately limited as predicted by the study of local spatial frequency in equation 3.22. By Fourier transforming this function and by performing some changes of variables the spectrum of $g(x, y)$ for the x coordinate is:

$$G_x(f_x) = \frac{e^{-i\pi \frac{f_x^2}{\alpha}}}{\sqrt{2\alpha}} \left\{ C\left[\sqrt{2\alpha}\left(L_x - \frac{f_x}{\alpha}\right)\right] - C\left[\sqrt{2\alpha}\left(-L_x - \frac{f_x}{\alpha}\right)\right] \right. \\ \left. + iS\left[\sqrt{2\alpha}\left(L_x - \frac{f_x}{\alpha}\right)\right] - iS\left[\sqrt{2\alpha}\left(-L_x - \frac{f_x}{\alpha}\right)\right] \right\} \quad (3.23)$$

where C and S represent the so called Fresnel integrals [10]:

$$C(x) = \int_0^x \cos\left(\frac{\pi t^2}{2}\right) dt \quad S(x) = \int_0^x \sin\left(\frac{\pi t^2}{2}\right) dt \quad (3.24)$$

From figure 3.1 it is possible to notice that the spectrum is almost flat outside of the $(-L_x, L_x)$ region so in this case the spatial frequency provides an indication of where the Fourier spectrum will have non negligible values. This is true for those cases where the phase distribution $\phi(x, y)$ varies slowly in the (x, y) plane. For these cases, from the local spatial frequency it is possible to estimate where significant values of the Fourier spectrum will be located making it possible to estimate the necessary sampling frequency to well reconstruct a signal when Fourier transforming it. This concept will be exploited in the next section.

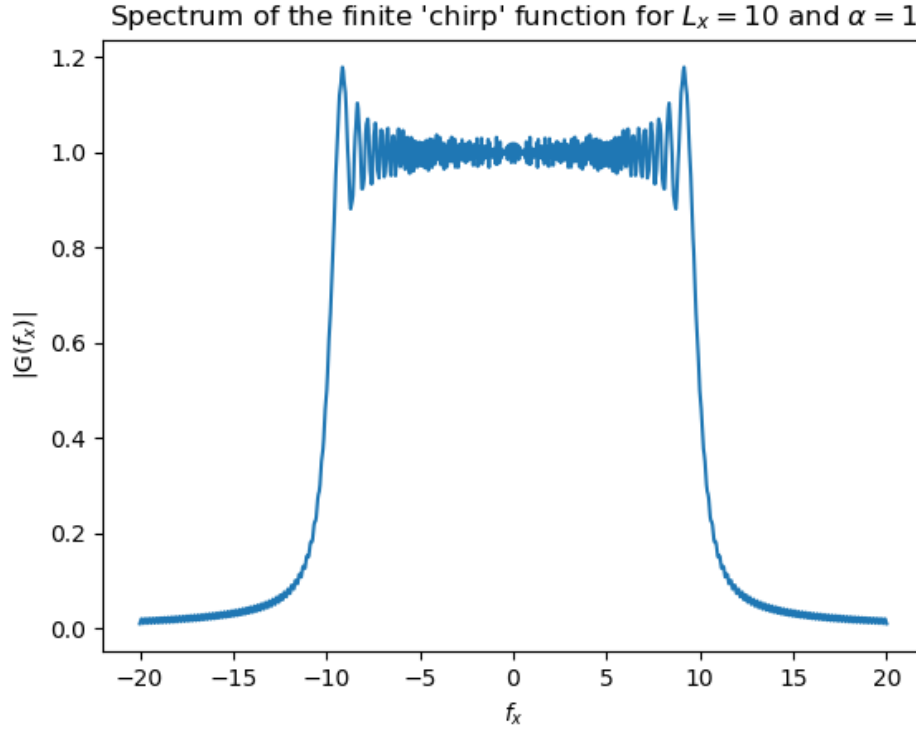


Figure 3.1: Spectrum of the 'chirp' function multiplied for a rect function of width $L_x = 10$ and $\alpha = 1$. As it possible to notice it assumes non negligible values only between roughly $(-10, 10)$.

From Fourier transform to discrete Fourier transform

Because complex cases of propagation in free-space require the use of computer, there is the necessity to develop a Fourier analysis theory that deals with discretization: to represent a function $g(x, y)$ with a computer it is, in fact, necessary to sample it with a discrete number of values. Obviously, the more samples are taken, the closer the discretized function $g(x_n, y_n)$ will resemble the continuous one, with the drawback being an increase of computing resources needed. First a definition of discrete-Fourier-transform is given, then a study of the sampling theory is done following the work of J. D. Schmidt [11]. At the end of this discussion the foundations necessary to develop a theory of diffraction of light in free-space and a way to simulate it with numerical calculations will have been laid.

In order to discretize the Fourier transform as defined in equation 3.12 the integral must be re-written as a Riemann sum:

$$G(f_{xm}) = \mathcal{F}\{g(x_n)\} = \sum_{n=-\infty}^{\infty} g(x_n) e^{-i2\pi f_{xm} x_n} (x_{n+1} - x_n), \quad m = -\infty, \dots, \infty \quad (3.25)$$

with m and n integers. However, computers can only store a finite number of samples N . From now on δ will identify an homogeneous sampling interval and so the spatial coordinate becomes $x_n = n\delta$. Frequency interval is then defined as $\delta_f = \frac{1}{N\delta}$ [12] and, again, $f_{xm} = m\delta_f = \frac{m}{N\delta}$. Equation 3.25 becomes:

$$G\left(\frac{m}{N\delta}\right) = \mathcal{F}\{g(n\delta)\} = \delta \sum_{n=-\frac{N}{2}}^{\frac{N}{2}-1} g(n\delta) e^{-i2\pi \frac{mn}{N}}, \quad m = -\frac{N}{2}, 1 - \frac{N}{2}, \dots, \frac{N}{2} - 2, \frac{N}{2} - 1 \quad (3.26)$$

The same approach can be followed to find the inverse discrete Fourier transform. DFT can be performed with many algorithms [12]: in this work we use the fast Fourier transform (*FFT*) function implemented in the library Numpy of Python.

Choosing the right grid spacing δ and the number of samples N is a fundamental issue for an accurate calculation of Fourier transform. The Shannon theorem states that a bandlimited signal having no spectral components above f_{max} is completely determined by giving its ordinates at a series of grid points spaced at most $\delta_c = \frac{1}{2f_{max}}$. In other words the requirement is to have at least two samples per period for the highest frequency component of the signal.

The discretization brings many benefits in term of applicability when using computer simulations but also some drawbacks: the limited number of samples and the finite spatial and spatial-frequency domain grid leads to aliasing, blurring and smearing in the spatial-frequency domain and in the spatial domain. Following closely the approach of Schmidt [11] and E. Oran Brigham [13] a clear explanation of the effects of the discretization and windowing is now given through the construction of the DFT starting from the continuous FT. Consider a continuous function $g(x)$ and its transform $G(f_x)$:

$$g(x) = e^{-a|x|}$$

$$G(f_x) = \frac{1}{a} \frac{2}{1 + \left(\frac{2\pi f_x}{a}\right)^2} \quad (3.27)$$

as an example to show discretization effect easily generalizable to all other functions.

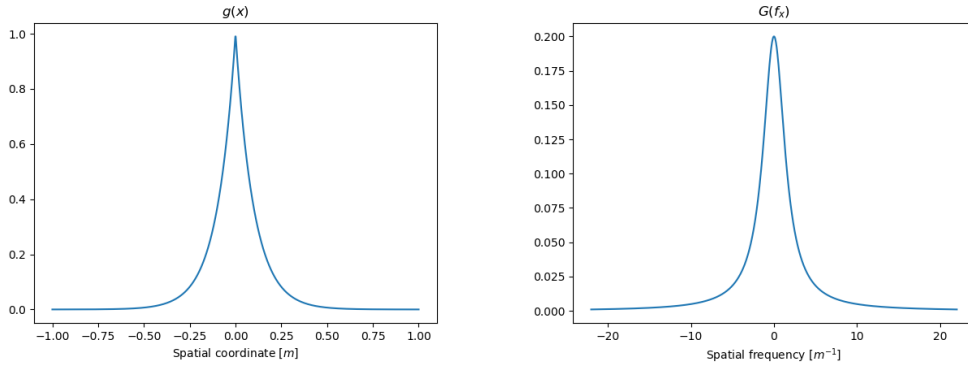


Figure 3.2: Graph of example continuous function $g(x)$ and it Fourier transform $G(f_x)$

The first operation to perform is the sampling that can be described mathematically multiplying the function $g(x)$ with a comb of delta functions spaced δ from each other. As was said before (cf.3.15) a multiplication of two function in one space corresponds to the convolution of the two functions Fourier transformed in the conjugate space:

$$g(x) \frac{1}{\delta} \text{comb}\left(\frac{x}{\delta}\right) \Leftrightarrow G(f_x) * \text{comb}(\delta f_x) \quad (3.28)$$

As it is possible to see in figure 3.3 the result of sampling is a periodic replica of the G function separated by a distance $\frac{1}{\delta}$. This is called **aliasing** and it wouldn't be visible if the sampling rate satisfies the requirement of the Shannon theorem for bandlimited functions because the replicas would be further apart, out of the sampling window.

The next effect to be considered is the finite number N of samples that can be taken. Windowing corresponds to considering the g function multiplied for a rect function that truncates the tails:

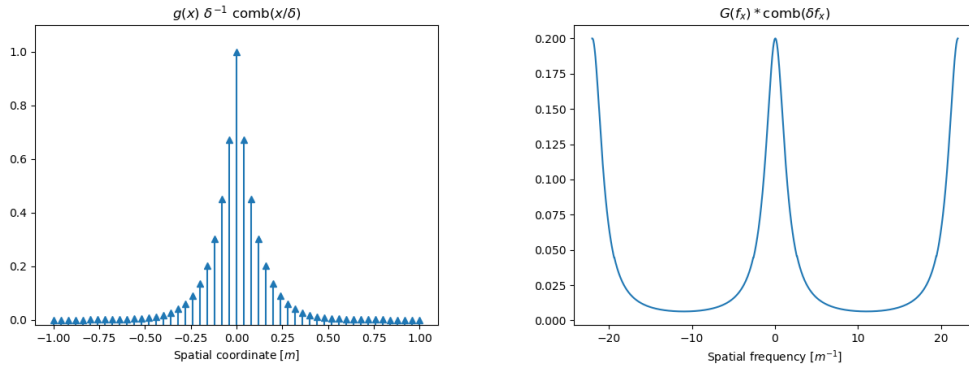


Figure 3.3: The graph shows the result of a discrete sampling of function $g(x)$ and the aliasing effect in the spatial-frequency domain caused by an insufficient sampling rate.

$$g(x) \frac{1}{\delta} \text{comb}\left(\frac{x}{\delta}\right) \text{rect}\left(\frac{x}{L}\right) \Leftrightarrow G(f_x) * \text{comb}(\delta f_x) * [L \text{sinc}(L f_x)] \quad (3.29)$$

The result is a cut in the tails of the function g beyond the area occupied by the square and a convolution operation between the result of equation 3.28 and a sinc function with blurring and smearing effect appearing like is visible in figure 3.4.

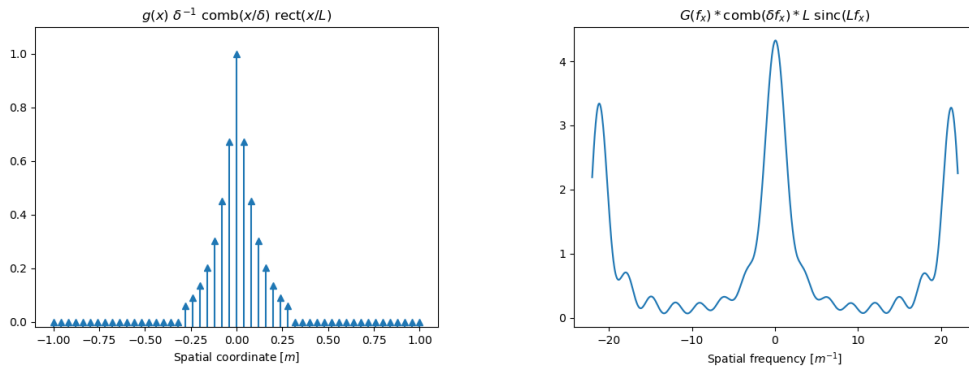


Figure 3.4: The graph shows the result of a finite number of samples taken for the function $g(x)$ and the blurring effect in the spatial-frequency domain caused by windowing the spatial interval $[-0.3, 0.3]$.

The resultant function $G(f_x)$ is still not acceptable because it is continuous; to face this problem, it is necessary to introduce a discretization effect by multiplying the spectrum for a comb of δ functions, like it was done for $g(x)$ in equation 3.28. As before, multiplying for a comb of δ functions corresponds to:

$$\tilde{g}(x) = \left[g(x) \frac{1}{\delta} \text{comb}\left(\frac{1}{\delta}\right) \text{rect}\left(\frac{x}{\delta}\right) \right] * \left[\frac{1}{L} \text{comb}\left(\frac{x}{L}\right) \right] \quad (3.30)$$

and:

$$\tilde{G}(f_x) = [G(f_x) * \text{comb}(\delta f_x) * [L \text{sinc}(L f_x)]] \text{comb}(L f_x) \quad (3.31)$$

An aliasing effect would be expected in the spatial domain because of the convolution with the comb function, exactly like in figure 3.5, however because the Fourier transform operation is done onto $g(x)$ to get $G(f_x)$ this replicas can't affect the input and remain 'virtual'. In figure 3.5 the aliasing is shown but it wouldn't be visible when only Fourier transforming. This is not true if an operation of inverse Fourier transformation is immediately following; in this case the discretization of the spectrum would cause real problem of aliasing in the spatial domain. As we will show later in the discussion, this matter is very important in our case because the propagator that we have developed works exploiting a Fourier transform and an inverse Fourier transform in series. So the appearance of "virtual" replicas in the spatial domain after the inverse Fourier transform will actually be seen if the sampling theorem is not satisfied for the spatial frequency domain.

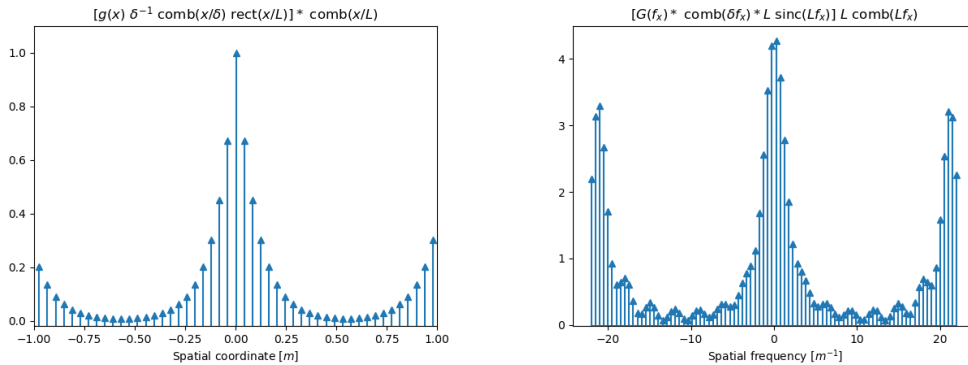


Figure 3.5: The graph shows the result of a finite number of samples taken for the function $G(f_x)$ and the aliasing effect in the spatial domain. Notice that this effect is visible only if the $g(x)$ is obtained from the function $G(f_x)$ via inverse DFT.

Knowing the drawbacks introduced by the sampling of a continuous function, it is possible to briefly address the problem of how to mitigate them. Aliasing is reduced by reducing the sampling step of $g(x)$ so that the replicas of $G(f_x)$ are further apart, out of the output win-

dow. While the blurring can be attenuated by enlarging the sampling window. By doing so the sinc function better approximate an impulse function and the convolution gives no blurring. To achieve both results a finer grid and wider window is required: this can be obtained by interpolating and by "zero padding" respectively. Zero padding is a simple method that adds a series of 0 values at the border of the window. Unfortunately this means of improving the results requires using more computer resources, both for memory and computational power.

Scalar electromagnetic theory

In this chapter the basics of classical electrodynamics theory of diffraction in free-space is discussed. The aim of the following pages is to derive the wave equations that governs the evolution of electromagnetic fields in free space. From Maxwell equations we derive the vacuum wave equation that describes the spatial and temporal evolution of electromagnetic fields in free space. We introduce the approximation of scalar theory: in this approximation the electromagnetic disturbance is not described by electric and magnetic field vectors at each point in time and space but rather by a single complex number. Once the time-dependent vacuum wave equation for scalar field is obtained, the field is described as a superposition of monochromatic waves, called spectral decomposition taking into consideration the theory of linear systems and of Fourier analysis mentioned in previous chapters (cf. 3.1 and 3.2). Each monochromatic component of the decomposition of the electromagnetic field will be shown to obey the Helmholtz equation, a time-independent form of the free space wave equation. We will focus our attention on the study of diffraction of waves obeying the Helmholtz equation in free-space, and in particular on the case of Fresnel diffraction. All this arguments will be discussed taking into consideration the studies of D. Paganin [14] from the point of view of the angular spectrum formulation, that, as was said before, represents the electromagnetic field as a superposition of monochromatic plane waves with different spatial frequency and direction of propagation.

We start from Maxwell wave equations:

$$\begin{aligned}
\nabla \times \mathcal{B} &= \epsilon_0 \mu_0 \frac{\partial \mathcal{E}}{\partial t} && \text{Faraday's law} \\
\nabla \times \mathcal{E} &= -\frac{\partial \mathcal{B}}{\partial t} && \text{Ampère's law} \\
\nabla \cdot \mathcal{B} &= 0 && \text{Gauss' law} \\
\nabla \cdot \mathcal{E} &= 0 && \text{Coulomb's law}
\end{aligned} \tag{3.32}$$

where \mathcal{B} is the magnetic induction, \mathcal{E} is the electric field, μ_0 and ϵ_0 are the magnetic and the electric permittivity of free-space, respectively, $\nabla \times$ is the curl operator and $\nabla \cdot$ is the divergence operator. The vacuum wave equation that governs the spatial and temporal evolution of the electromagnetic field in free space will be derived. Note that $\mathcal{E} = \mathcal{E}(x, y, z, t)$ and $\mathcal{B} = \mathcal{B}(x, y, z, t)$ are functions of four variables. To proceed further into obtaining the free-space wave equation for the electric field the following relations comes in handy:

$$\nabla \times [\nabla \times \mathbf{f}] = \nabla[\nabla \cdot \mathbf{f}] - \nabla^2 \mathbf{f} \tag{3.33}$$

with $\mathbf{f} = \mathbf{f}(x, y, z)$ a vector field. Applying $\nabla \times$ to the second of equations 3.32 and the relation just mentioned above:

$$\nabla[\nabla \cdot \mathcal{E}] = \nabla^2 \mathcal{E} + \frac{\partial}{\partial t} \mathcal{B} \tag{3.34}$$

Because the space is considered free of charge, the first term of equation 3.34 vanishes, then by rearranging terms and using Ampère's law (cf. equation 3.32) we obtain:

$$\left(\epsilon_0 \mu_0 \frac{\partial^2}{\partial t^2} - \nabla^2 \right) \mathcal{E} = \mathbf{0} \tag{3.35}$$

which is the d'Alembert wave equation for electric field. Applying the same approach yields to the vacuum field equation for the magnetic induction:

$$\left(\epsilon_0\mu_0\frac{\partial^2}{\partial t^2} - \nabla^2\right)\mathcal{B} = 0 \quad (3.36)$$

Note that since the vector Laplacian acts on the individual field components in the same way and keeping them uncoupled, the above vector equations, when projected onto x , y , or z direction, split into 6 identical uncoupled equations, one for each field component:

$$\begin{aligned} \left(\epsilon_0\mu_0\frac{\partial^2}{\partial t^2} - \nabla^2\right)\mathcal{E}_x(x, y, z, t) &= 0 \\ \left(\epsilon_0\mu_0\frac{\partial^2}{\partial t^2} - \nabla^2\right)\mathcal{E}_y(x, y, z, t) &= 0 \\ \left(\epsilon_0\mu_0\frac{\partial^2}{\partial t^2} - \nabla^2\right)\mathcal{E}_z(x, y, z, t) &= 0 \end{aligned} \quad (3.37)$$

This is known as the scalar wave equation:

$$\left(\frac{1}{c^2}\frac{\partial^2}{\partial t^2} - \nabla^2\right)U(x, y, z, t) = 0 \quad (3.38)$$

where the scalar $U(x, y, z, t)$ stands for any of the three component of the vector fields \mathcal{E} and \mathcal{B} and $c = \frac{1}{\sqrt{\mu_0\epsilon_0}}$ is the speed of light in vacuum. This equations show that the electric and magnetic field that compose light are traveling wave fields. If we consider one propagation direction z , the electric field reduces to two components in direction perpendicular to z : $\mathcal{E}_\sigma(x, y, z = z_0, t)$ $\mathcal{E}_\pi(x, y, z = z_0, t)$. \mathcal{E}_σ and \mathcal{E}_π describe the two components of polarized light. If we ignore polarization, we can drop the vectorial description and consider $\mathcal{E}(x, y, z = z_0, t)$ as a scalar so the description of the electromagnetic field is now done with a scalar theory, which means that the electromagnetic disturbance is not described by two vectors, the electric field and the magnetic field, but by a single scalar field, function of position and time. Because the field functions are linear, solutions with different frequencies can be added to form wave-packet solutions. For this reason, fields with harmonic time dependence $e^{-i\omega t}$ are those studied in the following chapters. When substituting such field into equation 3.38, the result is:

$$\left[\nabla^2 + \left(\frac{\omega}{c} \right)^2 \right] U(x, y, z, t) = 0 \quad (3.39)$$

and considering $k = \frac{2\pi}{\lambda}$ the wavenumber corresponding to a wavelength λ , $\omega = 2\pi f$ the angular frequency of the radiation corresponding to frequency f and $c = \lambda f$ the speed of light in vacuum the previous equation becomes:

$$[\nabla^2 + k^2] U(x, y, z) = 0 \quad (3.40)$$

This is the Helmholtz equation, and in reason of the condition upon which it has been found, only considering time harmonic fields, it shows that the time dependence can be factorized and not used for this type of functions. In fact, the time solution for such equation is always the same while the spatial solution depends on the initial and boundary conditions. From here on the time dependency of the field $U(x, y, z)$ is not written. It is now possible to work with a complex scalar function that obeys the Helmholtz equation.

Scalar diffraction theory

When the optical source is not a simple wave (e.g. plane or spherical), solving the scalar Helmholtz equation is not trivial so we need to use more sophisticated mathematical tools, like the Green's theorem with clever use of the boundary conditions. However, here, another more intuitive approach is followed. Exact and approximate methods for solving diffraction problems based on the Helmholtz equation will be shown. This method is called angular spectrum or plane-wave decomposition and it is developed in a framework that closely resembles the theory of linear systems (cf. chapter 3.1). It has the advantage of being more intuitive and free from some of the subtle difficulties of boundary conditions encountered when solving the Helmholtz equation exploiting the Green's theorem while (cf. Goodman [8]).

Angular spectrum method

Consider the case of a source that emits only in the half-space where the coordinate z of the Cartesian system that describes its position is $z > 0$. The space is supposed to be free of electric charges and a monochromatic wave only is considered to propagate forward with respect to the z coordinate. Stated this, the angular spectrum formalism permits to construct an operator which applied to the electric field of incident wave permits to calculate the propagated one over any plane parallel to the initial one downstream of the source. Starting with the previous Cartesian coordinate system (x, y, z) , where the axis z in the positive direction is considered to be the optical axis, consider two parallel planes, $z = 0$ and $z = \Delta z$ where Δz is a positive value on the z -axis. Consider the space between the two planes to be in vacuum, which means that equation 3.40 is here obeyed. The aim is to use such equation to get an explicit form of the operator that once applied to the forward propagating field $U(x, y, 0)$ yields to the propagated wave-field $U(x, y, \Delta z)$ at the plane $z = \Delta z$. A simple example of propagation can be achieved with the special case of a plane wave forward propagating along the z -axis:

$$U^{(PW)}(x, y, z) = e^{i(k_x x + k_y y + k_z z)} \quad (3.41)$$

This waves are solution of the Helmholtz equation provided that:

$$k_x^2 + k_y^2 + k_z^2 = k^2 \quad (3.42)$$

where k_x, k_y, k_z are respectively the three components of the wave-vector \mathbf{k} of the wave. This vector gives the direction of propagation of the wave and has a magnitude $k = \frac{2\pi}{\lambda}$. Expressing k_z as a function of k , k_x and k_y and taking the positive square root value which, as before, makes it so only propagation in the positive direction of the z -axis is considered:

$$k_z = \sqrt{k^2 - k_x^2 - k_y^2} \quad (3.43)$$

By substituting equation 3.43 into equation 3.41:

$$U^{(PW)}(x, y, z) = e^{i(k_x x + k_y y)} e^{iz\sqrt{k^2 - k_x^2 - k_y^2}} \quad (3.44)$$

Now the plane wave at position $z = 0$ is

$$U^{(PW)}(x, y, 0) = e^{i(k_x x + k_y y)} \quad (3.45)$$

The trivial problem of diffraction for a plane wave has then been solved. In fact, to obtain the propagated wave field it simply a matter of multiplying the unpropagated disturbance by the propagation factor $e^{iz\sqrt{k^2 - k_x^2 - k_y^2}}$, that will be called 'free space propagator'. Extending this result from a plane wave forward propagating in vacuum between two parallel planes at position $z = 0$ and $z = \Delta z$ to a more general disturbance is a matter of expressing the general unpropagated wave field as a linear combination of plane waves through the use of two dimensional Fourier integral (cf. chapter 3.1):

$$U(x, y, 0) = \frac{1}{2\pi} \int \int \tilde{U}(k_x, k_y, 0) e^{i(k_x x + k_y y)} dk_x dk_y \quad (3.46)$$

where $\tilde{U}(k_x, k_y, 0)$ denotes the Fourier transform of $U(x, y, 0)$ with respect to x and y while k_x and k_y represent the spatial-frequencies coordinate in the Fourier space. By applying the propagator operator $e^{iz\sqrt{k^2 - k_x^2 - k_y^2}}$ to the unpropagated field, as it was show before, it is possible to retrieve the value of the field $U(x, y, \Delta z)$ propagated by a distance $z = \Delta z$. In order to do so, it is necessary to multiply such propagator for every component in which the unpropagated field as been decomposed through the use of equation 3.46, (cf. 3.9, thus getting:

$$U(x, y, \Delta z) = \frac{1}{2\pi} \int \int \tilde{U}(k_x, k_y, 0) e^{i\Delta z\sqrt{k^2 - k_x^2 - k_y^2}} e^{i(k_x x + k_y y)} dk_x dk_y \quad (3.47)$$

This is the **angular-spectrum representation** for propagated fields and it provides a rigorous solution to a certain boundary problem of the Helmholtz equation, namely one in which a forward propagation happens in free-space between two parallel planes.

We are interested to study the propagation of synchrotron radiation, a coherent X-ray beam that propagates making only small angles with respect to the z -axis. In this case the wave field is said to be 'paraxial'. In this special case, an approximation of the equation 3.47 leads to a simpler solution to the Helmholtz equation equivalent to the famous Fresnel diffraction integral. Starting from the previous general result, suppose that $U(x, y, 0)$ is now a scalar function that describes a paraxial wave field. Since the paraxiality, as mentioned before, imply that all the non-negligible plane-wave components of the forward propagating field have small wavenumber components k_x and k_y such that $k_z \ll k_x, k_y$, it is possible to expand with Taylor expansion the square-root argument of the exponential of the free-space propagation:

$$\sqrt{k^2 - k_x^2 - k_y^2} \approx k - \frac{k_x^2 + k_y^2}{2k} \quad (3.48)$$

The propagated paraxial field is then described by a approximate form of the free-space propagator, called the Fresnel propagator:

$$U(x, y, \Delta z) = \frac{1}{2\pi} \int \int \tilde{U}(k_x, k_y) e^{ik\Delta z} e^{\frac{-i\Delta z(k_x^2 + k_y^2)}{2k}} e^{i(k_x x + k_y y)} dk_x dk_y \quad (3.49)$$

It is possible to demonstrate that the angular spectrum formalism developed here and the Rayleigh-Sommerfeld diffraction integral of the first kind yield identical predictions of diffracted fields. This was done elegantly by Sherman [15] and Lalor [16].

Wavefront propagator and implementations

Chapter 3 led to finding an exact solution to the boundary-value problem of propagation of a wavefront between two parallel planes in free space in the paraxial approximation. At this point, it is necessary to recast the expression in a way that let us solve it numerically by the use of *FFT* [17]. This algorithm is necessary especially for 2D simulations in optics. If we consider a wavefront sampled in $N \times N$ pixels (being $N \gtrsim 10^3$), when calculating the 2D integrals to propagate the wavefront to another plane with the same resolution, we need approximately $N^2 \cdot N^2 \approx 10^{12}$ operations. This implicate the necessity of a great amount of storage and calculations not feasible for normal computers. When performing the same calculations taking advantage of the theory of Fourier optics, one *FFT* requires $\approx N^2 \log_2 N \approx 10^7$ operations [18]. This is the reason why we seek for a form that let us exploit such powerful tool. By looking at equation 3.49 it is possible to write it in a form that resemble a convolution in two dimensions:

$$f(x, y) * g(x, y) := \int_{-\infty}^{\infty} \int_{-\infty}^{\infty} f(x', y') g(x - x', y - y') dx' dy' \quad (4.1)$$

And by making use of the two-dimensional form of the convolution theorem (cf. eq. 3.15):

$$f(x, y) * g(x, y) = \mathcal{F}^{-1} \{ \mathcal{F}\{f(x, y)\} \times \mathcal{F}\{g(x, y)\} \} \quad (4.2)$$

equation 3.49 can be written as:

$$\begin{aligned} U(x, y, \Delta z) &= \mathcal{F}^{-1} \left\{ \mathcal{F}\{U(x, y, 0)\} \times \frac{e^{ik\Delta z}}{2\pi} e^{\frac{-i\Delta z(k_x^2 + k_y^2)}{2k}} \right\} \\ &= \mathcal{F}^{-1} \left\{ \mathcal{F}\{U(x, y, 0)\} \times \mathcal{F}\mathcal{F}^{-1} \left\{ \frac{e^{ik\Delta z}}{2\pi} e^{\frac{-i\Delta z(k_x^2 + k_y^2)}{2k}} \right\} \right\} \end{aligned} \quad (4.3)$$

This equation represents now a convolution:

$$U(x, y, \Delta z) = U(x, y, 0) * h(x, y) \quad (4.4)$$

where

$$h(x, y) := \frac{1}{2\pi} e^{ik\Delta z} \mathcal{F}^{-1} \left\{ e^{\frac{-i\Delta z(k_x^2 + k_y^2)}{2k}} \right\} \quad (4.5)$$

is the Fresnel propagator in real-space form in the paraxial approximation. In order to recast equation 3.49 in a way that resemble the convolution form of equation 4.1, we need to obtain the explicit form of the real space Fresnel propagator by performing the inverse Fourier transform operation that appears in equation 4.5:

$$\begin{aligned} h(x, y) &= \frac{e^{ik\Delta z}}{4\pi^2} \int_{-\infty}^{\infty} \int_{-\infty}^{\infty} e^{\frac{-i\Delta z(k_x^2 + k_y^2)}{2k}} e^{i(k_x x + k_y y)} dk_x dk_y \\ &= \frac{e^{ik\Delta z}}{4\pi^2} \int_{-\infty}^{\infty} e^{i(k_x x - \frac{\Delta z}{2k} k_x^2)} dk_x \int_{-\infty}^{\infty} e^{i(k_y y - \frac{\Delta z}{2k} k_y^2)} dk_y \end{aligned} \quad (4.6)$$

By doing a change of variable of integration from k_x to $\kappa := [k_x - \frac{k_x}{\Delta z}] \sqrt{\frac{\Delta z}{\pi k}}$ we obtain:

$$\begin{aligned} \int_{-\infty}^{\infty} e^{i(k_x x - \frac{\Delta z}{2k} k_x^2)} dk_x &= e^{\frac{ik_x^2}{2\Delta z}} \int_{-\infty}^{\infty} e^{-\frac{i\Delta z}{2k} (k_x - \frac{k_x}{\Delta z})^2} dk_x \\ &= 2\sqrt{\frac{\pi k}{2\Delta z}} e^{\frac{ik_x^2}{2\Delta z}} \int_0^{\infty} e^{-i\frac{\pi}{2} \kappa^2} d\kappa \\ &= \sqrt{\frac{2\pi k}{\Delta z}} e^{i(\frac{k_x^2}{2\Delta z} - \frac{\pi}{4})} \end{aligned} \quad (4.7)$$

Note that the last expression is obtained considering that the integral in κ of the second row of equation of equation 4.7 is equal to $\frac{1}{2}(1 - i) = \frac{e^{-i\frac{\pi}{4}}}{\sqrt{2}}$. The same expression is found for k_y and rearranging the result we get:

$$h(x, y) = -\frac{ik e^{ik\Delta z}}{2\pi\Delta z} e^{\frac{ik(x^2+y^2)}{2\Delta z}} \quad (4.8)$$

that is the explicit real form of the Fresnel propagator. Getting back to equation 4.4 and substituting the real form of Fresnel propagator and writing explicitly the convolution operation:

$$\begin{aligned} U(x, y, \Delta z) &= -\frac{ik e^{ik\Delta z}}{2\pi\Delta z} \left\{ U(x, y, 0) * e^{\frac{ik(x^2+y^2)}{2\Delta z}} \right\} \\ &= \frac{e^{ik\Delta z}}{i\lambda\Delta z} \int_{-\infty}^{\infty} \int_{-\infty}^{\infty} U(x', y', 0) e^{i\frac{k}{2\Delta z}[(x-x')^2+(y-y')^2]} dx' dy' \end{aligned} \quad (4.9)$$

It may be useful to briefly summarize how to perform the calculation of propagation listing the three necessary steps:

1. Fourier transform the unpropagated field: $\mathcal{F}\{U(x, y, 0)\}$
2. multiply it for the free-space Fresnel propagator $e^{\frac{-i\Delta z(k_x^2+k_y^2)}{2k}}$
3. inverse Fourier transform with respect to k_x and k_y the result of step (2): $\frac{e^{ik\Delta z}}{2\pi} \mathcal{F}^{-1}\{\}$

The result is:

$$U(x, y, \Delta z) = \mathcal{F}^{-1}\left\{ \mathcal{F}\{U(x, y, 0)\} e^{ik\Delta z} e^{\frac{-i\Delta z(k_x^2+k_y^2)}{2k}} \right\} \quad (4.10)$$

Expression of equation 4.10 is suitable to be calculated numerically with the use of Fast Fourier Transform algorithm (FFT) simply swapping the Fourier transform operator $\mathcal{F}\{\}$ with the discrete Fourier transform one FFT , taking into account the sampling conditions discussed in chapter 3.3:

$$U(x, y, \Delta z) = \frac{e^{ik\Delta z}}{2\pi} FFT^{-1}\left\{ FTT\{U(x, y, 0)\} \times e^{\frac{-i\Delta z(k_x^2+k_y^2)}{2k}} \right\} \quad (4.11)$$

This form of the Fresnel propagator is the one usually used for the simulation of the propagation of wavefronts. Software suites like Wofry [2] or PyNX [19] use it for the simulations.

Introduction of a magnification factor

Expression 4.11 provide a fast way of propagating a wavefront from the source plane to the observation plane; however it does not provide any mean of changing final pixel size. To perform numerically this expression, it is necessary to sample the source field and use discrete Fourier transform (DFT) such as *FFT* algorithm. Hence, there is no way to resolve a small spot, which can be obtained, for example, from the propagation of converging wavefront, with enough accuracy but by sampling the input with a very fine grid. The consequence is the need of a powerful computer and a long time to perform the calculus. For this reason we have exploited a simple mathematical expedience, the addition of a magnification factor m in the previous formula, to give the possibility to modify the spacing grid at the image plane. The apparent effect is to be able to look at propagated wavefront with a zoom. Following the approach of J. Schmidt [11], the quadratic argument of the exponential that appears in equation 4.9 is modified in order to introduce a magnification factor. However, because optical elements used at synchrotron beamlines have usually uncorrelated effects for vertical and horizontal direction, (e.g. mirrors focusing only along one direction or rectangular aperture) we modify both the $(x - x')^2$ and the $(y - y')^2$ terms to introduce two magnification factors m_x and m_y , that act independently for the two coordinates x and y . Here the procedure is shown only for the x variable, but the same must be done for the y variable as well:

$$\begin{aligned}
 (x_2 - x_1)^2 &= x_2^2 + x_1^2 - 2x_1x_2 \\
 &= x_2^2 + \frac{x_2^2}{m_x} - \frac{x_2^2}{m_x} - 2x_1x_2 + x_1^2 + m_x x_1^2 - m_x x_1^2 \\
 &= \frac{x_2^2}{m_x} + \left(1 - \frac{1}{m_x}\right)x_2^2 - 2x_2x_1 + \left[m_x x_1^2 + (1 - m_x)x_1^2\right] \\
 &= m_x \left[\left(\frac{x_2}{m_x}\right)^2 - 2\left(\frac{x_2}{m_x}\right)x_1 + x_1^2\right] + \left(1 - \frac{1}{m_x}\right)x_2^2 + (1 - m_x)x_1^2 \\
 &= m_x \left(\frac{x_2}{m_x} - x_1\right)^2 + \left(\frac{m_x - 1}{m_x}\right)x_2^2 + (1 - m_x)x_1^2 \tag{4.12}
 \end{aligned}$$

A change of name for the coordinate is done with respect to expressions appearing before equation 4.12 to better highlight that the final coordinate x_2 is a rescaled version of the initial

coordinate x_1 . Moreover, coordinate z is now dropped since (x_2, y_2) unequivocally identify the coordinate of the propagated field. Substituting this expression in equation 4.9:

$$U(x_2, y_2) = \frac{e^{ik\Delta z}}{i\lambda\Delta z} \int_{-\infty}^{\infty} \int_{-\infty}^{\infty} U(x_1, y_1) e^{i\frac{k}{2\Delta z} [m_x(\frac{x_2}{m_x} - x_1)^2 + (\frac{m_x-1}{m_x})x_2^2 + (1-m_x)x_1^2]} e^{i\frac{k}{2\Delta z} [m_y(\frac{y_2}{m_y} - y_1)^2 + (\frac{m_y-1}{m_y})y_2^2 + (1-m_y)y_1^2]} dx_1 dy_1 \quad (4.13)$$

and factoring out of the integral what does not depend on the integration variables we get:

$$U(x_2, y_2) = \frac{e^{ik\Delta z}}{i\lambda\Delta z} e^{i\frac{k}{2\Delta z} [(\frac{m_x-1}{m_x})x_2^2 + (\frac{m_y-1}{m_y})y_2^2]} \int_{-\infty}^{\infty} \int_{-\infty}^{\infty} U(x_1, y_1) e^{i\frac{k}{2\Delta z} [m_x(\frac{x_2}{m_x} - x_1)^2 + (1-m_x)x_1^2]} e^{i\frac{k}{2\Delta z} [m_y(\frac{y_2}{m_y} - y_1)^2 + (1-m_y)y_1^2]} dx_1 dy_1 \quad (4.14)$$

By making a change of variables

$$U''(x_1, y_1) = U(x_1, y_1) e^{i\frac{k}{2\Delta z} [(1-m_x)x_1^2 + (1-m_y)y_1^2]} \quad (4.15)$$

$$U(x_2, y_2) = \frac{e^{ik\Delta z}}{i\lambda\Delta z} e^{i\frac{k}{2\Delta z} [(\frac{m_x-1}{m_x})x_2^2 + (\frac{m_y-1}{m_y})y_2^2]} \int_{-\infty}^{\infty} \int_{-\infty}^{\infty} U''(x_1, y_1) e^{i\frac{k}{2\Delta z} [m_x(\frac{x_2}{m_x} - x_1)^2]} e^{i\frac{k}{2\Delta z} [m_y(\frac{y_2}{m_y} - y_1)^2]} dx_1 dy_1 \quad (4.16)$$

and defining the scaled coordinates

$$\begin{aligned} x'_2 &= \frac{x_2}{m_x} \\ y'_2 &= \frac{y_2}{m_y} \end{aligned} \quad (4.17)$$

$$U(m_x x'_2, m_y y'_2) = \frac{e^{ik\Delta z}}{i\lambda\Delta z} e^{i\frac{k}{2\Delta z}[(m_x-1)m_x(x'_2)^2 + (m_y-1)m_y(y'_2)^2]} \int_{-\infty}^{\infty} \int_{-\infty}^{\infty} U''(x_1, y_1) e^{i\frac{k}{2\Delta z}[m_x(x'_2-x_1)^2]} e^{i\frac{k}{2\Delta z}[m_y(y'_2-y_1)^2]} dx_1 dy_1 \quad (4.18)$$

a convolution form is again obtained:

$$U(m_x x'_2, m_y y'_2) = \frac{e^{ik\Delta z}}{i\lambda\Delta z} e^{i\frac{k}{2\Delta z}[(m_x-1)m_x(x'_2)^2 + (m_y-1)m_y(y'_2)^2]} \int_{-\infty}^{\infty} \int_{-\infty}^{\infty} U''(x_1, y_1) h_m((x'_2 - x_1), (y'_2 - y_1)) dx_1 dy_1 \quad (4.19)$$

where the function $h_m(x, y)$, which is now a scaled Fresnel propagator is defined as follows:

$$h_m(x_1, y_1) := \frac{1}{i\lambda\Delta z} e^{i\frac{k}{2\Delta z}[m_x x_1^2 + m_y y_1^2]} \quad (4.20)$$

At this point it is desirable to find the analytical Fourier transform of h_m to get a form that make it possible to apply equation 4.2:

$$\mathcal{F}_{x,y}[h_m(x, y)] = \frac{1}{\sqrt{m_x m_y}} e^{-i\pi\lambda\Delta z(\frac{f_x^2}{m_x} + \frac{f_y^2}{m_y})} \quad (4.21)$$

and by applying the convolution theorem:

$$\boxed{U(x_2, y_2) = \frac{e^{ik\Delta z}}{\sqrt{m_x m_y}} e^{i\frac{k}{2\Delta z}[\frac{m_x-1}{m_x}x_2^2 + \frac{m_y-1}{m_y}y_2^2]} \mathcal{F}^{-1}\left[\mathcal{F}[U(x_1, y_1)] e^{i\frac{k}{2\Delta z}[(1-m_x)x_1^2 + (1-m_y)y_1^2]} \times e^{-i\pi\lambda\Delta z(\frac{f_x^2}{m_x} + \frac{f_y^2}{m_y})}\right]} \quad (4.22)$$

Equation 4.22 represent the propagation of a wavefront $U(x, y)$ written in a form that is suitable to be computed again with *FFT* numerically by simply substituting the \mathcal{F} operation with the discrete one (*FFT*). Moreover, the introduction of an m factor gives the possibility

to act on the final spatial grid in order to zoom in and out. In the next chapter a physical interpretation will be given to this result obtained with a simple mathematical manipulation.

Physical interpretation

A physical interpretation of the consequences of the addition of two complex-exponential functions in Eq. 4.22, one that multiplies the initial wavefront $U(x_1, y_1)$ and one that only adds a phase term to the propagated wavefront, and the modification of the exponential responsible for the propagation, namely the Fresnel propagator, can be given on the basis of the 'Fresnel scaling theorem' described in Appendix B of Paganin's book [14]. Consider a monochromatic scalar wave propagating from a plane at position A in the negative region of a nominal optic axis z , to a plane in position $z = \Delta$. Suppose that the source is far enough so that the radiation can be considered paraxial, making the Fresnel approximation applicable. Consider the interaction with any element (i.e. a slit or a weakly scattering object) in position $z = 0$ that generates a diffraction pattern on the plane at position $z = \Delta$.

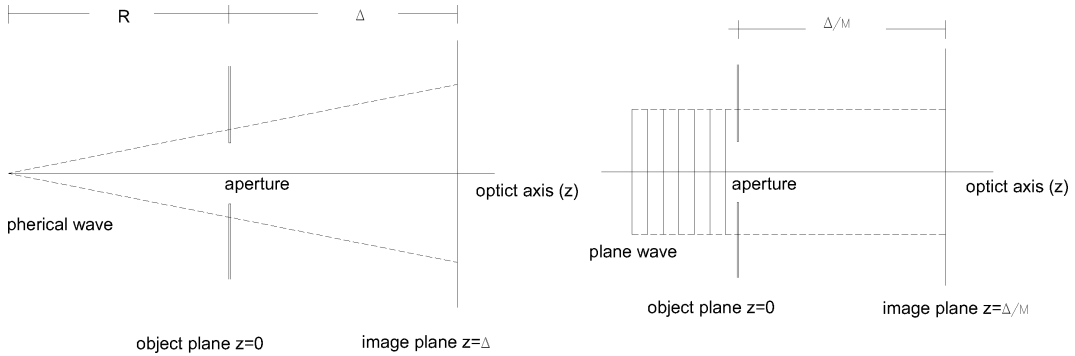


Figure 4.1: The schematics show the optical systems considered in the statement of the Fresnel scaling theorem. On the left a monochromatic point source, distant R from the object plane, emits X-Rays, that after passing through a slit at position $z = 0$ on the optical axis (z), generate a diffraction pattern on a plane at position $z=\Delta$. The geometric magnification of the image M is given by the relation $(R + \Delta)/R$. On the right the same system is illuminated by plane waves generating a diffraction pattern at a distance $z = \Delta/M$. The Fresnel scaling theorem states that the two diffraction patterns are identical provided that a rescaling of the complex amplitude and of the coordinates is performed.

Given these initial conditions the theorem states that, the Fresnel diffraction pattern will have a geometric magnification M which depends on the source-to-sample distance R , together with the sample-to-detector distance Δ . If we consider the limiting case of a source at an

infinite distance $R = \infty$, namely the case of a plane wave illuminating the object, we get a unit magnification. In this framework the Fresnel scaling theorem provides a simple mapping between the Fresnel diffraction pattern of an object which is obtained for the case of illumination by a point source, and a Fresnel diffraction pattern obtained for the limiting case of a plane-wave illumination. To retrieve the relation that links this two cases let's consider the plane-wave-illuminated Fresnel diffraction pattern, obtained over a plane at a propagation distance $z = \frac{\Delta}{M}$ downstream of the exit surface of the object and let's transversely magnify it by a factor M and finally multiply the result by a phase term and divide by a factor M . The derivation of this theorem provides an explanation of the effects of the mathematical manipulation introduced in the $2FFT$ propagator shown in the previous section (cf. equation 4.22).

Starting from equation 4.9 and recasting it in the form:

$$U^{(R)}(x, y, \Delta) = \frac{e^{ik\Delta}}{i\lambda\Delta z} e^{\left[\frac{ik}{2\Delta}(x^2+y^2)\right]} \int_{-\infty}^{\infty} \int_{-\infty}^{\infty} U^{(R)}(x', y', 0) e^{\frac{ik}{2\Delta}[(x')^2+(y')^2]} e^{\left[\frac{-ik}{\Delta}(xx'+yy')\right]} dx' dy' \quad (4.23)$$

where $U^{(R)}(x, y, \Delta)$ denotes the monochromatic scalar wave-field impinging over the plane $z = \Delta$ and the R superscript indicates the distance of the source from the object. Under the paraxial approximation the wavefront $U^{(\infty)}(x, y, 0)$ illuminating the object by a plane wave and $U^{(R)}(x, y, 0)$ illuminating the object by a spherical wave are related via:

$$U^{(R)}(x, y, 0) = U^{(\infty)}(x, y, 0) e^{\left[\frac{ik}{2R}(x^2+y^2)\right]} \quad (4.24)$$

Having written relation 4.24 between the unpropagated wave at the plane $z = 0$ for the case of the plane-wave illumination and the point-source illumination, it is possible to seek the relation between the complex-amplitude of the propagated fields:

$$U^{(R)}(x, y, \Delta) = \frac{e^{ik\Delta}}{i\lambda\Delta} e^{\left[\frac{ik}{2\Delta}(x^2+y^2)\right]} \int_{-\infty}^{\infty} \int_{-\infty}^{\infty} U^{(\infty)}(x', y', 0) e^{\left[\frac{ik}{2}(x'^2+y'^2)\left(\frac{1}{\Delta}+\frac{1}{R}\right)\right]} e^{\left[\frac{-ik}{\Delta}(xx'+yy')\right]} dx' dy' \quad (4.25)$$

To proceed further it necessary to specify the the form of the geometric magnification M :

$$M = \frac{R + \Delta}{R} \quad (4.26)$$

so that:

$$\frac{1}{\Delta} + \frac{1}{R} = \frac{1}{\Delta} \left(\frac{R + \Delta}{R} \right) = \frac{M}{\Delta} \quad (4.27)$$

substituting the above expression into equation 4.25 we arrive to:

$$U^{(R)}(x, y, \Delta) = \frac{e^{ik\Delta}}{i\lambda\Delta} e^{\left[\frac{ik}{2\Delta}(x^2+y^2)\right]} \int_{-\infty}^{\infty} \int_{-\infty}^{\infty} U^{(\infty)}(x', y', 0) e^{\left[\frac{ikM}{2\Delta}(x'^2+y'^2)\right]} e^{\left[\frac{-ik}{\Delta}(xx'+yy')\right]} dx' dy' \quad (4.28)$$

If we take the limit of $R \rightarrow \infty$ in the formula above, so that $M \rightarrow 1$, we see that:

$$U^{(\infty)}(x, y, \Delta) = \frac{e^{ik\Delta}}{i\lambda\Delta} e^{\left[\frac{ik}{2\Delta}(x^2+y^2)\right]} \int_{-\infty}^{\infty} \int_{-\infty}^{\infty} U^{(\infty)}(x', y', 0) e^{\left[\frac{ik}{2\Delta}(x'^2+y'^2)\right]} e^{\left[\frac{-ik}{\Delta}(xx'+yy')\right]} dx' dy' \quad (4.29)$$

In order to compare the two equations 4.28 and 4.29 and find the maps that link them let's make the two integrals match. First considering distance of propagation for the case of the plane wave to be $\Delta^{(\infty)} = \frac{\Delta^{(R)}}{M}$ (where the superscript in this case has been added to make clear which coordinate are taken into consideration in the two formulas) so that equation

4.29 becomes:

$$U^{(\infty)}\left(x, y, \frac{\Delta}{M}\right) = \frac{M e^{\frac{ik\Delta}{M}}}{i\lambda\Delta} e^{\left[\frac{ikM}{2\Delta}(x^2+y^2)\right]} \int_{-\infty}^{\infty} \int_{-\infty}^{\infty} U^{(\infty)}(x', y', 0) e^{\left[\frac{ikM}{2\Delta}(x'^2+y'^2)\right]} e^{\left[\frac{-ikM}{\Delta}(xx'+yy')\right]} dx' dy' \quad (4.30)$$

and then considering rescaled coordinates (x, y) so that $(Mx^{(\infty)}, My^{(\infty)}) = (x^{(R)}, y^{(R)})$:

$$U^{(\infty)}\left(\frac{x}{M}, \frac{y}{M}, \frac{\Delta}{M}\right) = \frac{M e^{\frac{ik\Delta}{M}}}{i\lambda\Delta} e^{\left[\frac{ik}{2\Delta M}(x^2+y^2)\right]} \int_{-\infty}^{\infty} \int_{-\infty}^{\infty} U^{(\infty)}(x', y', 0) e^{\left[\frac{ikM}{2\Delta}(x'^2+y'^2)\right]} e^{\left[\frac{-ik}{\Delta}(xx'+yy')\right]} dx' dy' \quad (4.31)$$

By easily check by direct substitution of the integrals in formulas 4.28 and 4.31:

$$U^{(R)}(x, y, \Delta) = \frac{1}{M} e^{\left[ik\Delta\left(1-\frac{1}{M}\right)\right]} e^{\left[\frac{ik}{2\Delta}(x^2+y^2)\left(\frac{M-1}{M}\right)\right]} U^{(\infty)}\left(\frac{x}{M}, \frac{y}{M}, \frac{\Delta}{M}\right) \quad (4.32)$$

By rewriting equation 4.22 showing a unique scaling factor m for direction x and y and changing the variable name from Δz to Δ we obtain:

$$U(x_2, y_2) = \frac{e^{ik\Delta}}{m} e^{\frac{ik}{2\Delta} \left[(x_2^2 + y_2^2) \left(\frac{m-1}{m} \right) \right]} \mathcal{F}^{-1} \left[\mathcal{F} \left[U \left(\frac{x_2}{m}, \frac{y_2}{m} \right) e^{\frac{ik}{2\Delta} [(1-m)(x_1^2 + y_1^2)]} \right] \times e^{-i\pi\lambda\Delta m \left(\frac{f_x + f_y}{m} \right)^2} \right] \quad (4.33)$$

The expression can be seen as the result of the Fresnel scaling theorem in the Fourier spatial-frequency domain. In fact, the Fourier transform of the unpropagated field, to which a new spherical phase term is added, is propagated to a distanced $m\Delta$ upon a rescaling of the coordinates of the spatial-frequency domain $\frac{f_x + f_y}{m}$. Taking into account a rescaling of the coordinates following the similarity theorem (cf. Eq. 3.14) so that a shrink in the spatial coordinated correspond to an expansion of the Fourier spatial-frequency coordinates and vice versa, the effect obtained is the propagation of the wavefront with a zooming effect.

Validity conditions

Equation 4.22, although very useful and very powerful, requires some studies to determine if aliasing and rippling will show in the image. Here, attention is focused at finding the suitable m factor for those cases in which the distance and the source spot (i.e. initial window size) are known. The validity of the formula is limited by the phase ramp in the two complex exponential present in both the Fourier transform and the inverse Fourier transform. Applying the Shannon theorem we determine the minimum sampling interval (ie. δ) necessary to sample the maximum Fourier spatial-frequency of the spectrum of the exponentials. Being the constraint $f_{max} = \frac{1}{2\delta}$ we exploit the concept of *local spatial frequency* previously mentioned in chapter 3.2 to approximately determine the maximum Fourier spatial-frequency of the Fourier spectrum of the exponentials. Considering the term that multiplies the initial wavefront $U(x, y)$ and the x variable only:

$$\left| \frac{1}{2\pi} \frac{\partial}{\partial x} \left[\frac{2\pi}{\lambda\Delta z} (1-m)x^2 \right] \right| < \frac{1}{2\delta_1} \quad (4.34)$$

where x is the spatial coordinate defined as $n\delta_1$, with $n = -\frac{N}{2}, 1 - \frac{N}{2}, \dots, \frac{N}{2} - 2, \frac{N}{2} - 1$ the index that identifies the n -th pixel, and δ_1 is the pixel size. Next it is required to calculate the derivative:

$$\left| \frac{2x}{\lambda\Delta z} (1-m) \right| < \frac{1}{2\delta_1} \quad (4.35)$$

and evaluate it where its magnitude is the greatest. Notice that the maximum frequency for the case of a complex exponential with a quadratic term in the argument is linked to the dimension of the window (cf. equation 3.22). This happens at the border of the window, when $x = \frac{N}{2}\delta_1$ and by substituting

$$\frac{1}{\lambda\Delta z} |1-m| 2 \frac{N}{2} (\delta_1)^2 < 1 \quad (4.36)$$

Moreover, because the wavefront to be propagated can indeed assume a negligible value

within the limits imposed by the window size, it is possible to reduce the maximum frequency to be well sampled by imposing that it occurs when $x = \frac{D_1}{2}$ where D_1 represents the maximum size of the spot. This is equivalent to reducing the width of the rect function in equation 3.21 making it possible to actually consider a smaller maximum frequency to sample:

$$\frac{1}{\lambda \Delta z} |1 - m| 2 \frac{D_1}{2} \delta_1 < 1 \quad (4.37)$$

This leads to the following condition on $m = \frac{\delta_2}{\delta_1}$ and thus on the pixel size of the image plane δ_2 :

$$\boxed{\delta_1 - \frac{\lambda \Delta z}{D_1} < \delta_2 < \delta_1 + \frac{\lambda \Delta z}{D_1}} \quad (4.38)$$

There is a final issue that needs to be discussed at this point. The phase of the unpropagated wavefront should be taken into account when determining the sampling condition for the first exponential, making sure that it varies slowly enough for the concept of local spatial frequency to still hold. In the simple case in which the wavefront propagated is a spherical wave or it is possible to retrieve a dominant spherical component so that $U(x, y)$ can be written as:

$$U(x, y) = U'(x, y) e^{i \frac{k}{2R} (x^2 + y^2)} \quad (4.39)$$

it can be easily added to the previous condition by considering that its effect is to add another quadratical term into the first Fourier transform with the result becoming:

$$\boxed{\left(1 + \frac{\Delta z}{R}\right) \delta_1 - \frac{\lambda \Delta z}{D_1} < \delta_2 < \left(1 + \frac{\Delta z}{R}\right) \delta_1 + \frac{\lambda \Delta z}{D_1}} \quad (4.40)$$

where R is positive for diverging beam. Until now the limits imposed by first exponential have been discussed; now it is required to analyze the effect of the second quadratic term that comes with the inverse Fourier transform operation. However, it must be taken into

account that conditions now apply to the spatial frequency space where the sampling interval is $\delta_f = \frac{1}{N\delta_1}$. As before:

$$\left| \frac{1}{2\pi} \frac{\partial}{\partial f_x} \left[\frac{-\pi\lambda\Delta z}{m} (f_x)^2 \right] \right| < \frac{N\delta_1}{2} \quad (4.41)$$

and calculating the derivative:

$$\lambda \frac{\Delta z}{m} f_x < \frac{N\delta_1}{2} \quad (4.42)$$

Like before the local spatial frequency is expected to be maximum at the edge of the spatial frequency grid where $f_x = \frac{N}{2}\delta_f = \frac{N}{2} \frac{1}{N\delta_1}$:

$$\lambda \frac{\Delta z}{m} 2 \frac{N}{2} \left(\frac{1}{N\delta_1} \right)^2 < 1 \quad (4.43)$$

which implies that:

$$\boxed{\delta_2 > \frac{\lambda\Delta z}{N\delta_1}} \quad (4.44)$$

This limit is often very strict since the spectrum of the wave field does not usually extend up to the borders so that the highly oscillating exponential term is multiplied by a function that drops to zero before the borders of the window (see fig. 5.10(a)). This means that the exponential of equation 3.21 is multiplied by an amplitude factor that tend to zero at the border, again decreasing the dimension of the rect function and leading to a smaller maximum non negligible frequency. An example will be shown in next chapter when the spectrum of a wavefront generated by a synchrotron source is analyzed in deeper detail.

Discussion and applications

When simulating the propagation of a wavefront using the computer calculated discrete Fourier transform many artifacts not related with the phenomenon of diffraction, but only due to a bad sampling, can appear in the final image. For this reason the conditions described in chapter 4.3 must be followed to obtain correct propagations. Before describing how such conditions were tested in order to give an experimental proof of the theory, it is worth mentioning what are the possible visible artifacts. Keep in mind that the specific propagator used in this work employs a Fourier transform and an inverse Fourier transform. Starting from the examples of chapter 3.3 where the effect of sampling was shown with analytical calculus for a function $g(x)$ and its Fourier transform $G(f_{xm})$, we now show the resulting effect of applying the FFT algorithm to a well sampled spectrum and to an aliased one. This is interesting to identify the resulting effects for this simple case in which the spectrum is very smooth. Real cases are unfortunately more complicated. In figure 5.1 we show the resulting inverse Fourier transform of the function $G(f_x)$ resulting from a good sampling of the function $g(x)$: the spectrum does not present any aliasing and it decreases to zero before the borders of the image. The case shown in figure 5.2, on the other hand, represents the

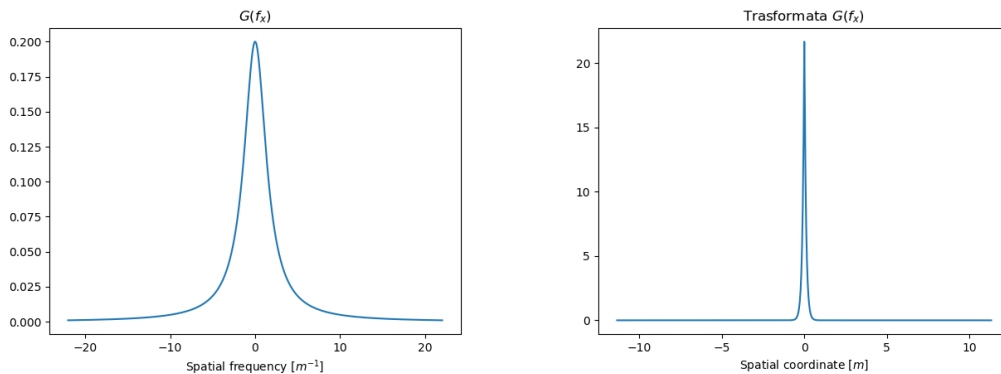


Figure 5.1: The graphs show a function $G(f_x)$ and its inverse Fourier transform calculated with FFT algorithm.

inverse Fourier transform for a function $G(f_x)$ that present an aliased spectrum.

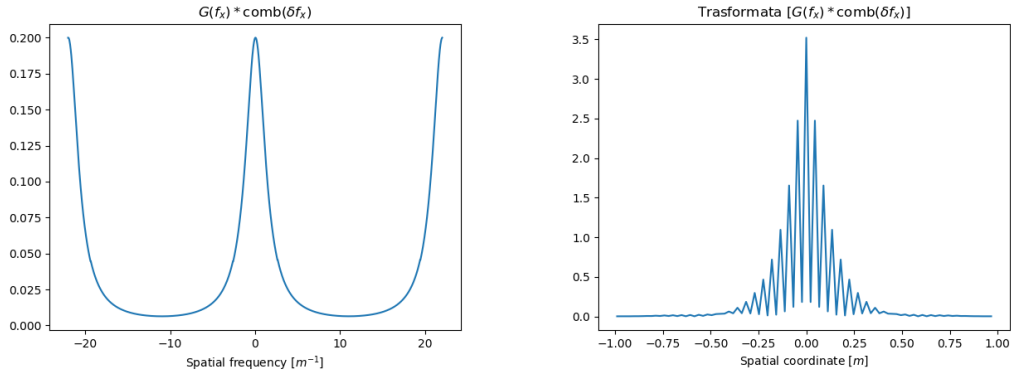


Figure 5.2: The graphs show a function $G(f_x)$ that presents some replicas and its inverse Fourier transform calculated with FFT algorithm. The effect of aliasing when Fourier transforming is visible comparing this result with the one of figure 5.1.

Aliasing conditions

In order to prove theoretical conditions 4.40 and 4.44 found in chapter 4.3, various test are performed to state whether a certain propagation includes aliasing figures and blurring. When building an optical system, the width of the object and image windows and the distance between them are known at least within a reasonable range, so, the test presented here are designed to highlight the correct values of m when trying to reproduce that particular optical system. As it was pointed out in chapter 3.3, both the width of the sampling interval (cf. equation 3.28) and the width of the window within which the wavefront is constrained (cf. 3.29) give tangible effects. The study of how this two factors affect the final simulation quality is done considering window sizes by looking at different coordinate values (x, y) in the same map and sampling interval by looking at the same value in the coordinate (x, y) for different maps. Each initial window size is represented by a value on the horizontal axis of maps like those in figure 5.4, while the vertical axis represents the dimension of the arrival window and, consequently, of the m factor used. The propagation of a wavefront, defined in a certain window and propagated to many different window sizes by changing the m parameter for each case, is represented by a vertical slice of the maps. To evaluate the rank for each propagation and make these maps, the resulting wavefront is compared point by point with a reference one, interpolated to fit the test windows size. The error is calculated with a method of least squares, summing the difference between the value of the curve at the

same coordinate. A bigger sum corresponds to a worse rank and a lighter color in the maps. This method makes detecting aliasing figures easy, especially considering the results in logarithmic scale, making it possible to study 100x100 propagations rapidly. Because the maps axes represent the windows size it is possible to perform this test sampling the wavefront with different number of points and comparing the results of more than one map. First, the system presented in the following schematic is considered. The results for this case, where

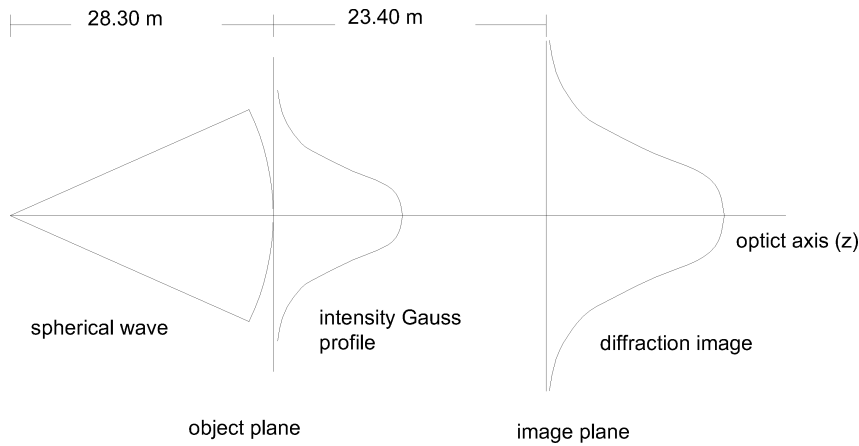


Figure 5.3: The schematic show the optical system used to generate the rank maps of figure 5.4. A point source at a distance of 28.3 m generates a wavefront of wavelength $\lambda = 0.73 \text{ \AA}$ upon which a Gaussian intensity profile is superimposed. The wavefront is propagated in free-space to a distance of 23.4 m. The Gaussian shapes shown in the schematic refers to the intensity profile of the wavefront at the two planes.

a spherical wavefront with radius of curvature $R = 28.3 \text{ m}$, wavelength $\lambda = 0.73 \text{ \AA}$ and a Gaussian intensity profile superimposed is propagated to a distance of 23.4 m from the sampling plane, are shown in Figure 5.4. A reference wavefront is compared with the same type of wavefront propagated with different magnification factors m and initial windows size. The reference wavefront is sampled with a greater amount of points than the test ones and with a larger window size to be able to easily interpolate it to match the desired dimension for every comparison. The Gaussian intensity profile is added not to have diffraction patterns at the borders of the figure that would come from windowing: this would make comparisons with the reference not possible. Two evaluations can be made: first, considering a vertical slice of the map, the right m factor can be determined for that specific initial window size, then comparing different maps the effect of a finer sampling interval is obtained. As it is possible to see from the maps a perfect matching between the theoretical conditions found

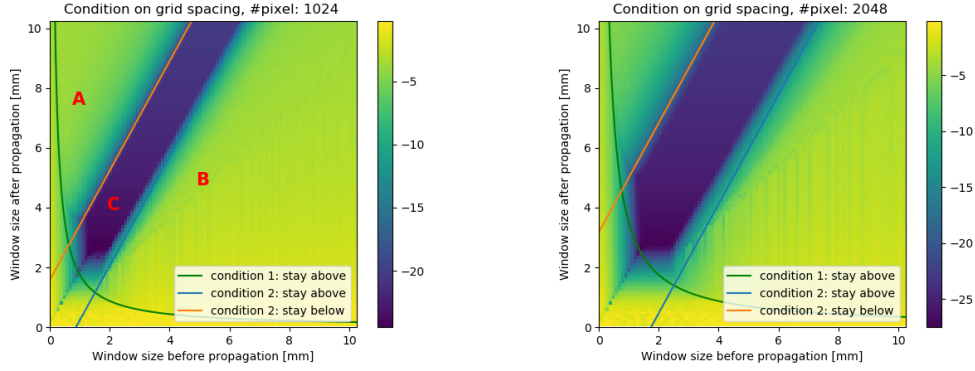


Figure 5.4: The images show the validity conditions as found with theoretical arguments (lines) and with simulations (image). Equation 4.44 refers to "condition 1" of the label (hyperbola), equation 4.40 to "condition 2" (straight lines). Spherical wavefronts with radius of curvature $R = 28.3 \text{ m}$ with a Gaussian intensity profile are propagate for a distance of 23.4 m . Figure 5.4(a) refers to the test done by sampling with 1024 point while figure 5.4(b) to one done sampling with 2048 points. Colors represents logarithmic values: blue for 'good' results, yellow for 'bad'. The three red letters in fig 5.4(a) are used in the following figures to show the results of the propagations corresponding to those zones in the map.

in chapter 4.3 and the results of simulation is obtained. "Condition 1" of the legend refers to the equation 4.41 while "condition 2" refers to equation 4.41. The dark colors indicate a good similarity between reference and test wavefront. Figure 5.4(a) and 5.4(b) correspond to the same test done with 1024 samples and 2048 respectively. The images show that with a greater amount of samples per figure the borders within which it is possible to have a well propagated wavefront greatly increases. This fact can be related to aliasing replicas being pushed further away from the central spot like it was mention when considering equation 3.28. It must be noticed that for small initial and final windows size, diffraction pattern are obtained at the extremities of the propagated field because the borders of the windows act as a slit. Because no analytical solution are available for the case analyzed here, a smooth reference wavefront generated by using a large windows size and a dense sampling grid in order to respect the condition discussed in chapter 3.3 is compared with each of the resulting wavefront obtained varying the m parameter. If a wavefront presents diffraction fringes due to the presence of a slit, results in the corresponding region are not trustworthy. This is visible when looking at the map near condition 1: colors in that region tend to become lighter even if validity conditions are satisfied. Figure 5.9, which compare the theoretical result obtained solving Fresnel integrals analytically for a plane wave that passes through a

slit, show that the dark colors of the map follow more precisely the one predicted theoretically. This will be better explained few paragraphs below. For each region indicated by the red letters in figure 5.4(a) the intensity profile of the wavefront propagated to different regions is presented to highlight the effect of a bad sampling that does not respect the validity conditions found in chapter 4.3. Figure 5.5(a) show the case of propagation for region "C": as it is possible to see the intensity profile is smooth and there are no artifacts visible. This is the direct consequence of a sampling done respecting the theoretical conditions. Figure 5.5(b) represent the intensity profile of a wavefront that is propagated with an m factor that makes it so the final pixel size δ_2 does not respect condition of equation 4.44. This case is very interesting because it shows that sometimes this condition is too strict; in fact, it considers as maximum frequency that need to be sampled correctly, the one that correspond to the frequency found at the borders. Because the actual maximum non-zero frequency of the spectrum is much smaller the condition results too strict and supposedly wrong parameters are actually perfectly fine. Figure 5.6 shows the case of a propagation that is done using an m factor such that the propagation conditions lies correspond to a point in the map of figure 5.4 that respects "condition 1", namely equation 4.44, but stay just below "condition 2" in region "B" of the map. "Condition 2" refers to equation 4.40 that was found when imposing a limit for δ_2 that permits to well sample the exponential that multiplies the unpropagated field in the propagator equation (cf. 4.22); Image 5.6(a) shows that when this condition is the spectrum appear some rippling that causes artifacts in the intensity shown in figure 5.6(a). When the conditions are not respected at all the spectrum appear completely aliased and blurred causing very bad propagated wavefronts. Figure 5.7 show an example for the case of propagation corresponding to region A and B.

Another test is performed considering the propagation of a plane wave of $\lambda = 1 \mu\text{m}$ through a slit of 2 mm and propagated to a distance of 0.1 m. We considered this case that is also discussed by Schmidt [11] to have a comparison with the results found in literature. In this case, instead of using a reference wave, the results are compared with the analytical solution found by solving the Fresnel integrals that were used in equation 3.24. A more accurate explanation is given by Goodman [8]. In this case the map in the blue region is not as homogeneous as before because the spikes of the diffraction pattern and the small amounts

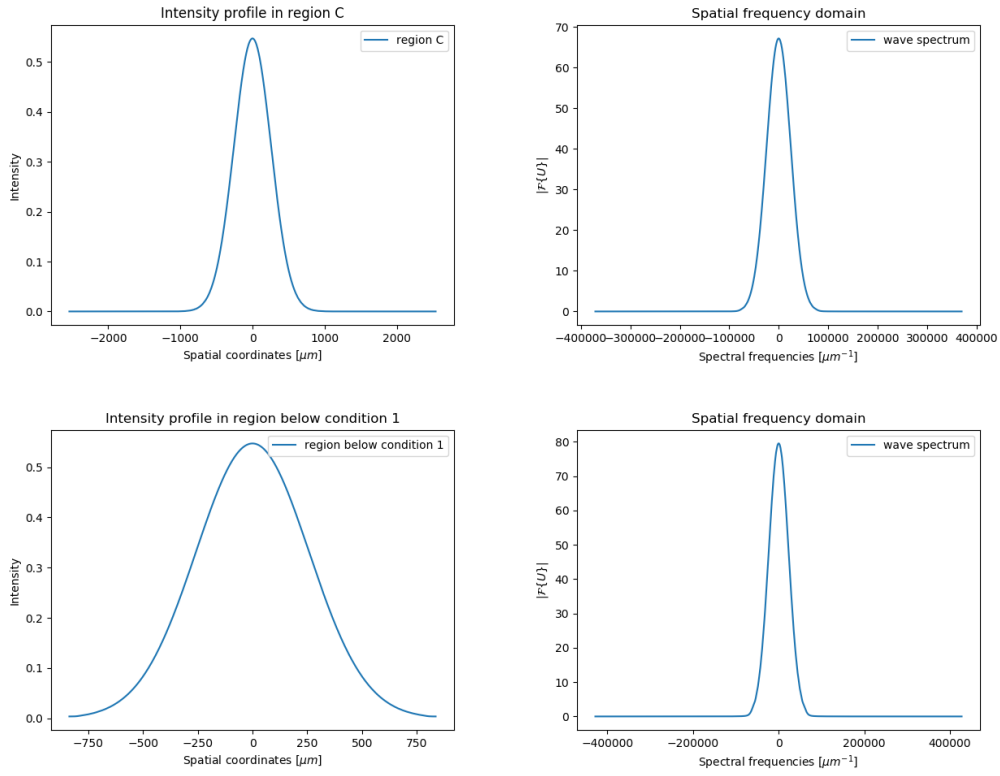


Figure 5.5: The images show the intensity profile of the wavefront propagated in the condition described by the schematic of figure 5.3. The top-left image show the intensity profile for a propagation corresponding to the zone "C" indicated in figure 5.4(a). The intensity show no presence of artifacts as it can be expected by looking at the spectrum shown in the top-left figure. The bottom-left box show the intensity profile of the wavefront propagated in the case in which condition "1" is not respected but condition "2" is. This case, shows that in some cases condition "1" can be too strict and that a good results can be obtained also when this is not perfectly respected.

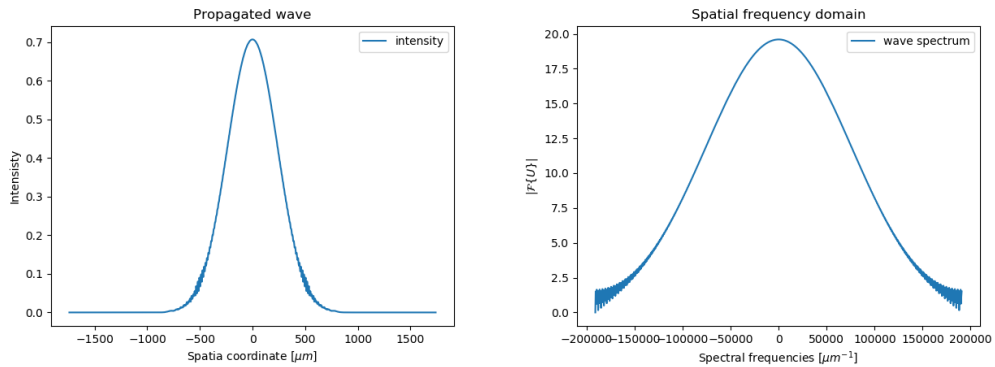


Figure 5.6: The images show the intensity profile of the propagated wavefronts in the case in which condition "2" are not respected perfectly. The propagation corresponds to the conditions highlighted by letter "B" in figure 5.4(a), when the parameter m is chosen to be just outside of the "good" blue zone. It is possible to see that in this case some artifacts appear in the intensity due to a bad sampling of the spectrum of the wavefront: aliasing and windowing effects are visible.

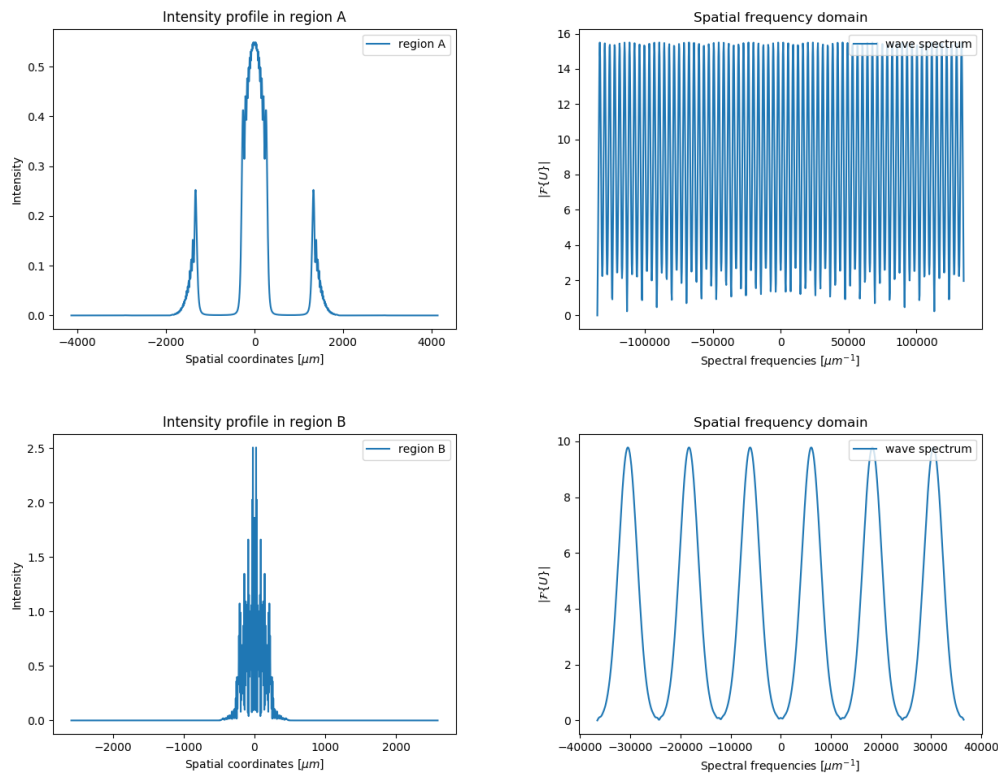


Figure 5.7: The images show the intensity profile of the propagated wavefronts in the case in which condition "2" are not respected at all. The propagation corresponds to the conditions highlighted by letter "A" and "B" in figure 5.4(a), respectively for top figures and bottom figures. It is possible to see that in this case artifacts cause the image to be completely different from the well propagated one shown in figure 5.5(a). A bad sampling of the spectrum of the wavefront is also visible.

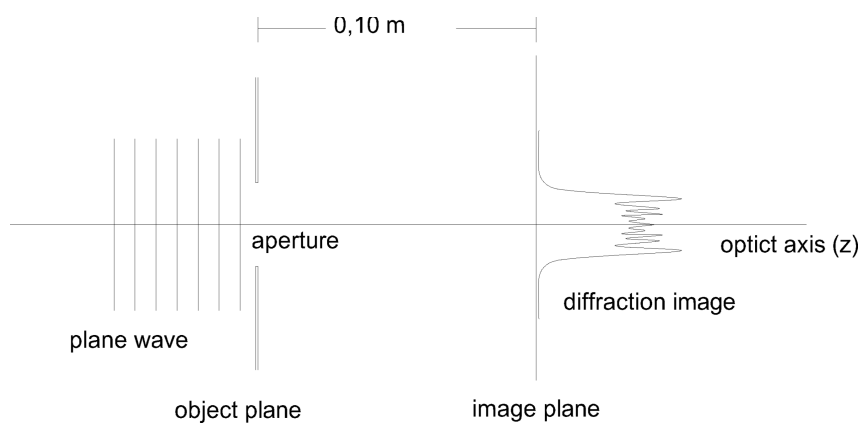


Figure 5.8: The schematic show the optic system used to show the validity condition found in chapter 4.3. A plane wave with a wavelength $\lambda = 1 \mu m$ is propagated through a slit of $2 mm$ at a distance of $0.1 m$. The pattern at the image plane indicate the intensity profile that is obtained.

of sampling points make it difficult to evaluate precisely the error. However it is clear that the behavior closely follows the one predicted theoretically. Again, to conclude the discussion

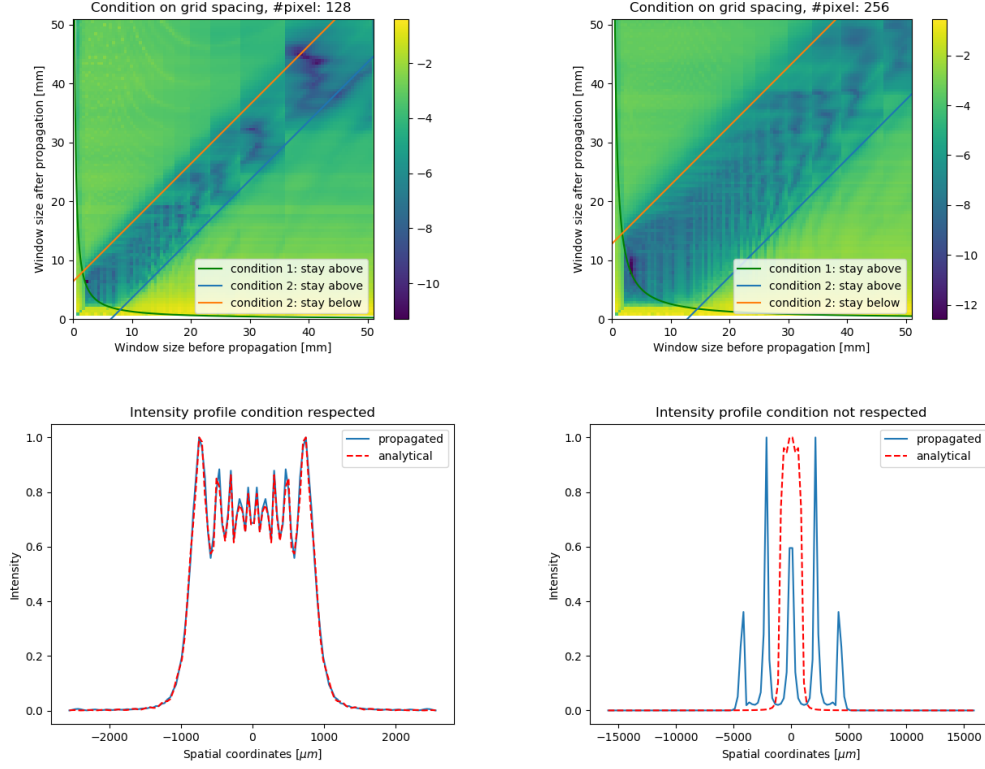


Figure 5.9: The images show the validity conditions when comparing a plane wave propagated through a slit with what is obtained with an analytical solution with the Fresnel integrals. Figures 5.9(a) and 5.9(b) show the map for a propagation done sampling with 128 and 256 pixels respectively. Graphs in figure 5.9(c) and 5.9(d) show an example of well propagated diffraction pattern and an aliased one.

on the limits of "condition 1" began when analyzing figure 5.5(b), figure 5.10 show the image of the spectrum of a wavefront propagated with parameters that belong to the region that stays below condition 1 in figure 5.9(b). In fact, as it has been explained before, the condition takes into account the maximum local frequency which is supposed to be linked with the maximal extension of the spatial frequency window. However, as it is clear from figure 5.10(a), since the spectrum decades quickly to zero before reaching the borders and since is multiplied by an highly oscillating exponential term, the contribution given by the higher frequency can be neglected making it possible to consider for example the maximum frequency for the Nyquist theorem to be halved or more. Finally, giving a closer look to equation 4.40 it is clear that "condition 2" strongly depends on the radius of curvature of the propagating wavefront. This dependence can be generalized for any phase associated to the

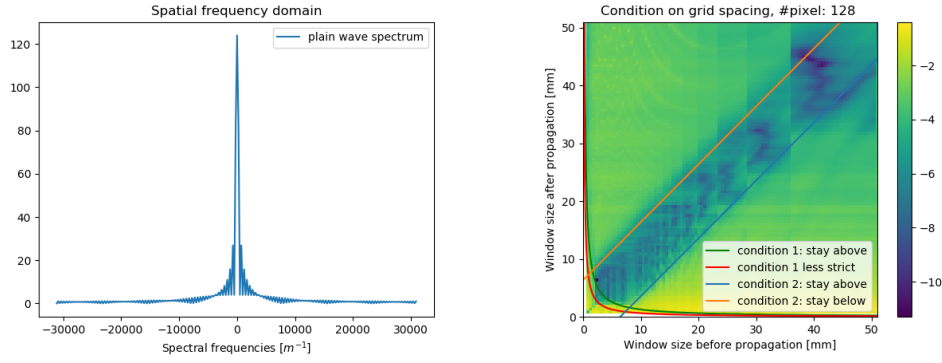


Figure 5.10: Figure 5.10(a) shows the spectrum of a plane that has passed through a slit, before it has been propagated. Since the spectrum assumes negligible values before the borders of the image, condition "1" corresponding to equation 4.44 is too strict since it considers the maximum value of the frequency to show at the borders. The images show the validity conditions when considering the actual spectrum is not as broad as it was supposed.

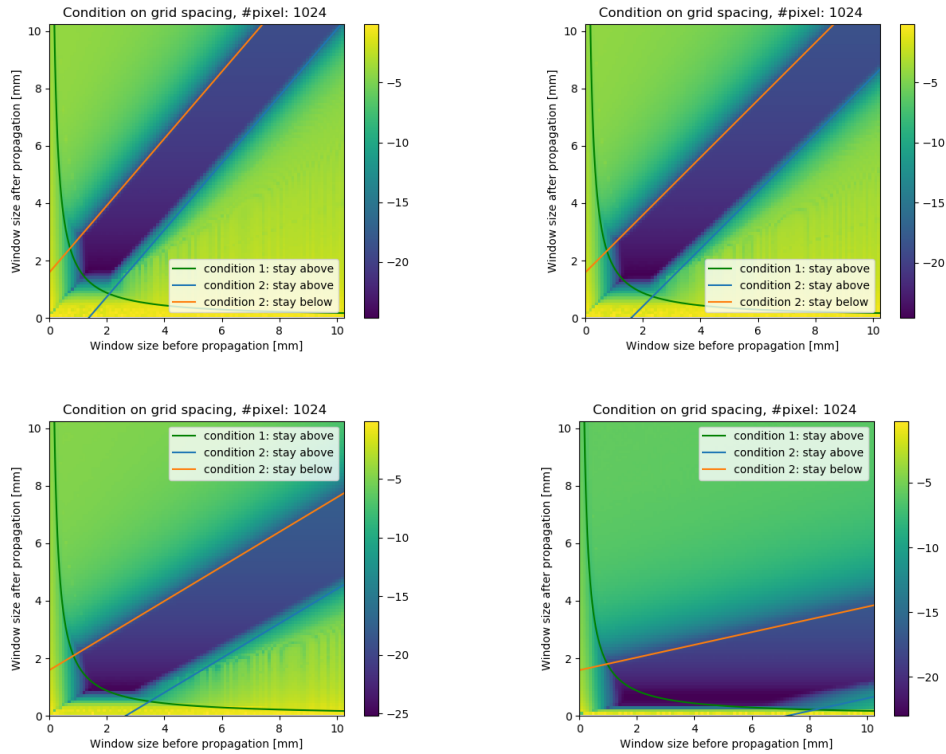


Figure 5.11: The images show the validity conditions for the case of propagation of wavefronts with different radius of curvature sampled with 1024 points. Eq. 4.40 shows the dependency of condition "2" on the radius of curvature of the input field. The four images refer to a propagation of 11.7 m for waves with $R = 141$ m (fig. 5.11(a)), $R = \infty$, so a plane wave, fig. 5.11(b)), $R = -58$ m (fig. 5.11(c)) and $R = -30$ m (fig. 5.11(d)).

unpropagated wavefront. Limiting the study to the simple presence of a spherical wave we see that changing the convergence makes the region corresponding to a good propagation move in the "space of the window size". The value of the radius of curvature of the beam determines the slope of the ideal line that fits the blue area. The results for different radius of curvature of the wavefronts are shown in Figure 5.11 for the same propagation distance and minimum and maximum window size.

The ESRF beamline ID16A

Once the validity conditions found with theoretic argumentation were proved to be correct with the tests described in previous section 5.1, a comparison between the simulation performed using the SRW software [20], as a base for the benchmark, and the angular spectrum propagator with zoom, integrated in the Wofry [2] library of Oasys [21], is presented in this chapter. SRW is used as a reference because it has been proven to be reliable by many benchmarks done over the past two decades in numerous synchrotron radiation facilities and is now widely accepted within the X-ray community. The chosen beamline is ID 16A at the ESRF, a last generation nanofocusing beamline, that presents a very peculiar and limit case: the high demagnification effect introduced by the set of mirrors makes it crucial to be able to well sample the final spot by changing pixel size along the propagation instead of using a very large number of points to define the source. Because the final light spot is several order of magnitude smaller than the source one, it requires a sampling interval much smaller than the initial one in order to appreciate all the diffraction fringes in detail. ID16A operates at three fixed photon energies: 11 200 eV, 17 225 eV and 33 600 eV, but only the second, which corresponds to the first harmonic of the undulator U18.3, is used for the simulations. The beamline is 185 m long and uses Kirkpatrick-Baez mirrors [22] to focus the beam. These mirrors are placed at a distance of few centimeters upstream the sample position. The monochromatization of light is obtained with a focusing multilayer monochromator. The effect of the ML is to create a secondary horizontal source at 40 m from the real source along the horizontal direction; this is clearer from the beamline schematic in Figure 5.12. The simulations are done assuming a fully coherent source and a propagation of the beam from element to element. Because the horizontal and vertical coupling of the beam

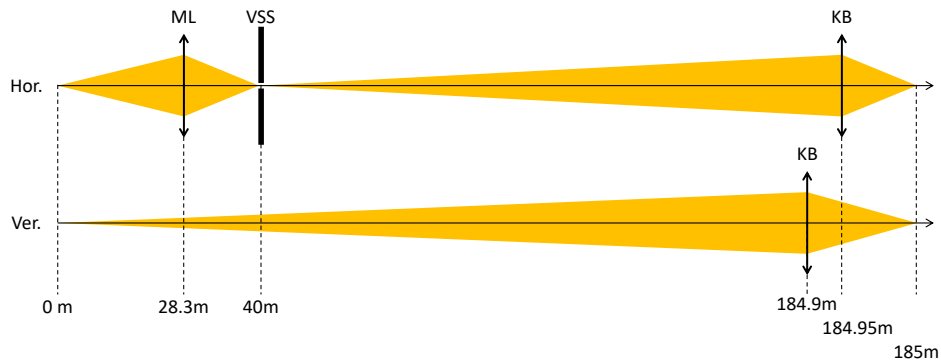


Figure 5.12: Schematic of ID16A for the horizontal (top) and vertical (bottom) planes. The main optical elements are visible in figure. ML stands for focusing multilayer monochromator while KB stands for Kirkpatrick-Baez focusing mirrors. VSS refers to the secondary horizontal source slit. The image is not in scale.

Position [m]:	Source	Multilayer	Slit	KB (v)	KB (h)	Focal plane
	0.00	28.30	40.00	184.90	184.95	185.00
Horizontal demag.:	-	2.42:1	-	-	2899:1	-
Vertical demag.:	-	-	-	1894:1	-	-

Table 5.1: Position of the main ID16A optical elements with respect to the undulator centre. Demagnification ($M^{-1} = p : q$, p = distance object-optics, q = distance optics-image) are also displayed power of the focusing elements is also shown.

is usually weak, the simulation has been split in two 1D ones for each plane to easily find the best propagation conditions. Moreover, each optical element is simplified by separating its effect in two phases: its finite size is obtained applying a slit while the focusing behavior is obtained with a thin lens. The source used is the on-axis-single electron emission from the undulator U18.3 tuned at its first harmonic at $E = 17\,225\text{ eV}$ simulated with the SRW software [7]. The intensity profiles at 28.3 m from the center of the undulator are visible in figure 5.13. This wavefront is then propagated through the various optical elements: first

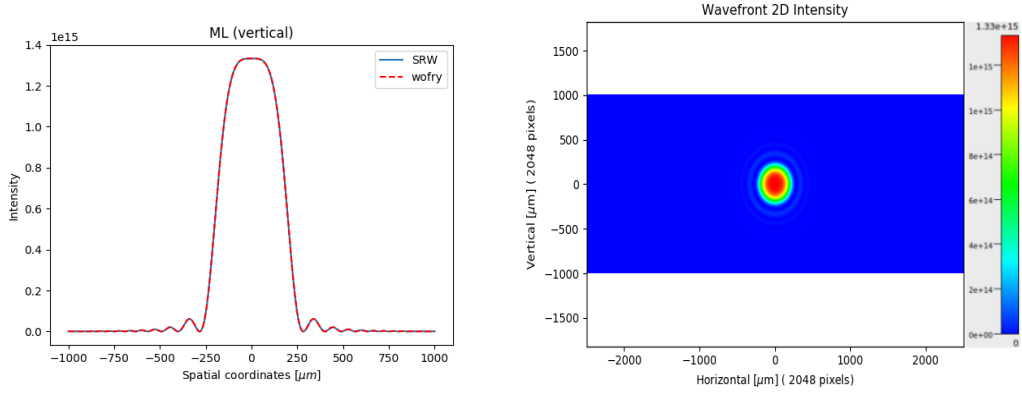
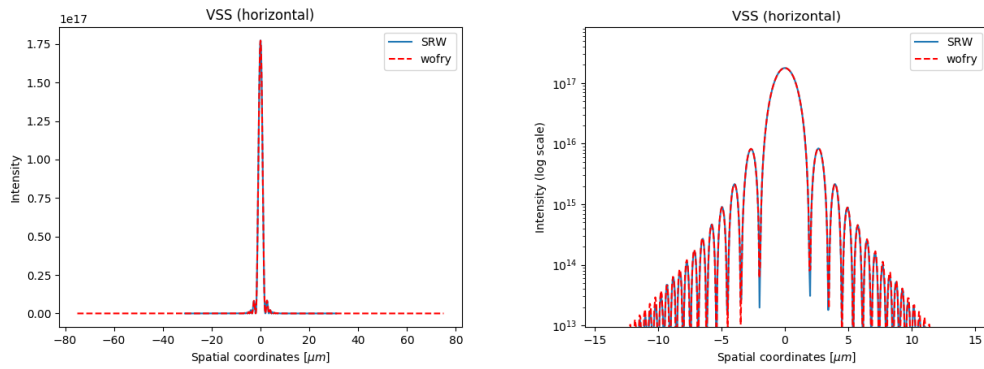
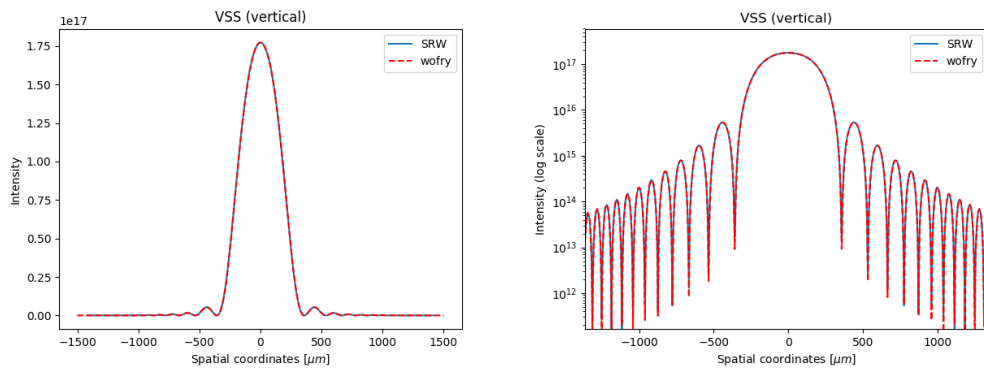


Figure 5.13: Intensity profiles (1D and 2D) of the wavefront generated by on-axis-single-electron emission from undulator U18.3

the monochromator that only focuses along the horizontal direction like it is shown in the schematics 5.12. In order to show the degree of similarity between the wavefronts propagated with Wofry and SRW, graphs with logarithmic scale on the vertical axis are also shown in figure 5.14. When the beam reaches the KB mirrors, a clipping occurs due to the acceptance of the elements. The effect is simulated by a slit before each element with horizontal and vertical dimension of $0.05 \times 0.000899\text{ m}$ and $0.00039 \times 0.013\text{ m}$ for the KBv and KBh respectively. The first slit has no effect along the horizontal direction as is clear from figure 5.15. However, as the beam is cut, the final spot results to be a diffraction pattern very similar to the one that would be obtained with a spherical wave diffracted by an aperture. Figure 5.16(a) and 5.16(b) represents the final spot size at the sample plane. It is possible to notice a clear similitude of the diffraction pattern. Simulations parameters for the propagation of the wavefront are summarized in table 5.2: In figure 5.17, taking into account the conditions of validity discussed in chapter 4.3, we show the limiting conditions to be respected not to have aliasing and the corresponding position in the "space of the windows size" for

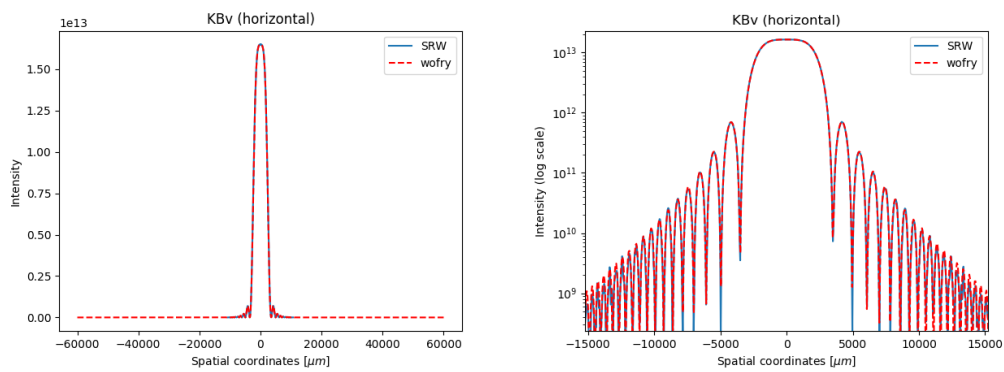


(a) VSS (horizontal)



(b) VSS (vertical)

Figure 5.14: Intensity profiles of wavefront at VSS plane (linear scale and logarithmic scale). Note that along the horizontal direction (top left image) the beam is focused.



(a) KBv (horizontal)

Figure 5.15: Intensity profile for the horizontal direction at KBv plane. Vertical direction and KBh planes are not shown because the finite size of the elements completely cuts the beam making the results not interesting for a comparison.

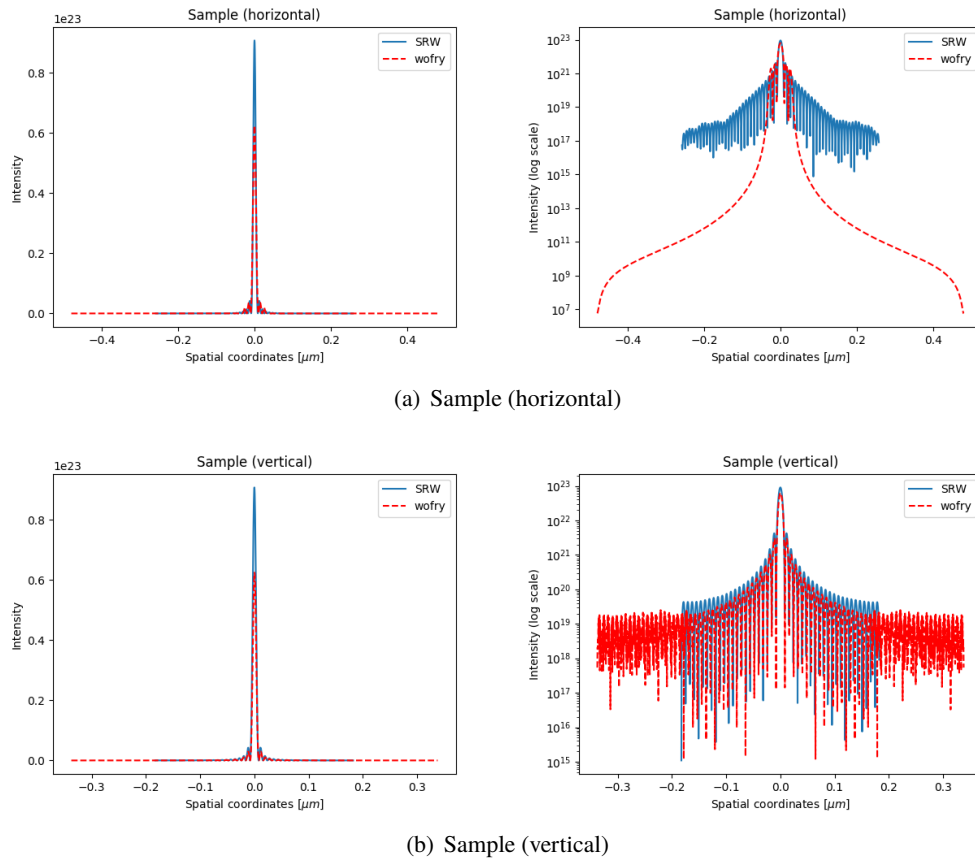


Figure 5.16: Comparison between intensity profiles at sample plane.

Element:	ML	VSS	KBv	KBh	sample
Position [m]:	28.3	40.00	184.90	184.95	185.00
H beam size [μm]:	800	9	14000	390	0.060
V beam size [μm]:	800	1800	899	450	0.080
H scaling factor:	1.0	0.03	800	1	0.000008
V scaling factor:	1.0	1.5	5	0.5	0.00009

Table 5.2: Beam sizes calculated for wave optics propagation of on-axis-single electron emission from the undulator and ideal lenses with aperture for modeling the element finite dimension.

the propagation to the VSS plane and the KBv plane. As it possible to see from such images the propagations belong to that the area has been identified to lead to propagation without artifacts.

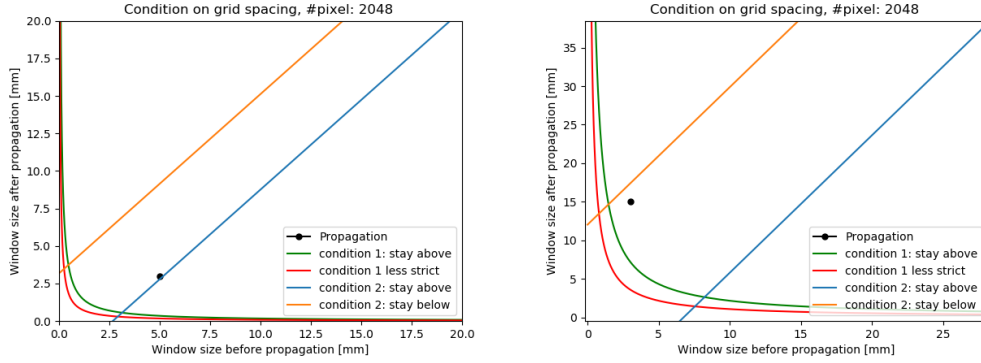


Figure 5.17: Example of position in the space of conditions for the simulation of the propagation from the ML plane to the VSS one (figure 5.17(a)) and from VSS plane to KBv plane (figure 5.17(a)) along the vertical direction.

Simulation of the effect of a decoherer system

The scaled propagator (cf. equation 4.22) was used by Caterina Amendola [23] (ID17 group at ESRF) in order to simulate the effect of a random phase scatter screen (also known as decoherer). The decoherer is used to reduce beam defects linked to the presence of several kind of optical elements. It consists of a rotating disk made of porous material, ranging from commercial sandpaper [24], [25] to porous nanoberyllium plate [26], which diffuse the radiation in all the directions. The aim of the experiments was to estimate the effect of the decoherer on optical system spatial resolution. Indeed, the decoherer generates a blurring in the images, which reduces the image quality. The blurring is measured as the FWHM of the Point Spread Function (PSF). In order to estimate the PSF, the Line Spread function (LSF) is computed as the first derivative of the Edge Spread Function (ESF), which was measured as intensity profile of tungsten blade. Measurement of the FWHM of LSF are taken both with and without the decoherer. The simulations are first compared with the measurements without the decoherer in order to estimate the detector's PSF. In the simulations the source is modeled as a coherent plane wave with Gaussian intensity profile of 20 μm of FWHM and a window size of 120 μm . The wavefront is propagated at the source-blade distance (ranging

from 145 m to 149.83 m) using the Wofry library. Finally, the wave transmitted by the blade is propagated at the detector-blade distance (ranging from 0.17 cm to 5 m). The PSF of the detector is estimated to be a Gaussian with a standard deviation of $2.67 \mu\text{m}$. From the simulated intensity profile obtained at the image plane, the calculated FWHM is shown in figure 5.18. From the simulations a distance (1.2 m) that minimizes the FWHM of the system can

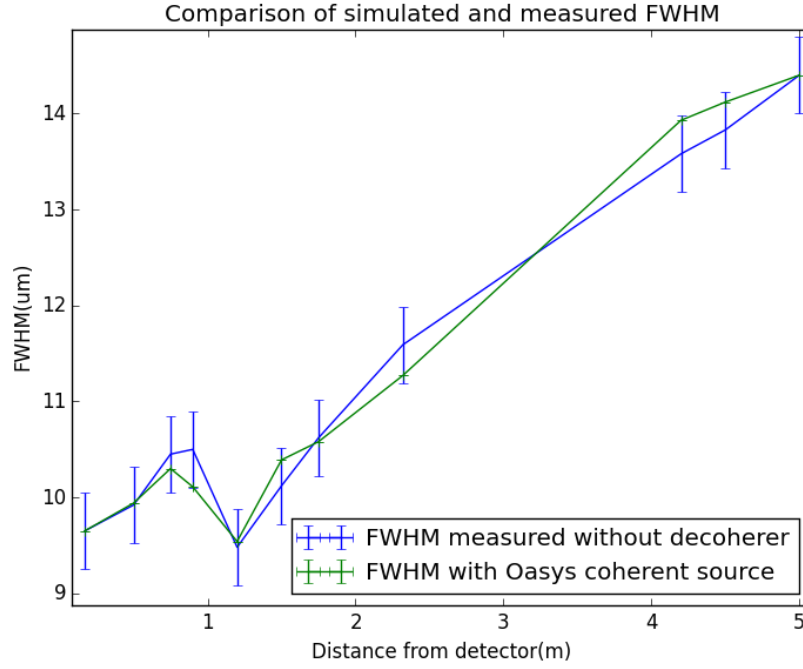


Figure 5.18: Comparison between FWHM measured and simulated without the decoherer. The simulations perfectly reproduce the experimental results, and the penumbra effect.

be observed. This behavior is related to the variation of width of the Fresnel diffraction fringes with the propagation distance and the dimension of the pixel size. In the simulations performed without binning, the sampling step size is $0.013 \mu\text{m}$, and Fresnel fringes are observed. The dimension of the first fringe, related to the maximum of interference, become higher than $3.07 \mu\text{m}$ (the pixel size dimension) for an object-detector propagation distance of 1.2 m. This variation of fringes dimensions, with respect to the pixel size ones, means that the integration performed due to the finite pixel size of the detector generates this effect of an increased (as in case of measure taken at 0.75 m and 0.9 m from the detector) or decreased (measure taken at 1.2 m from the detector) intensity, depending on the Fresnel fringes dimension that is observed in the values of the FWHM. The use of the simulations made it possible to formulate this model to explain a strange behavior that is due to the finite

pixel size of the detector. Having a numerous amount of simulated data that showed the Fresnel fringes for different distances of propagation made it possible to give this explanation. Once the FWHM of the detector's PSF was fixed at $2.67\text{ }\mu\text{m}$ and the validity of simulations is verified, a model of the decoherer effect has been studied. The phase variation induced by the decoherer is modeled as a random phase screen with Normal distribution [25]. The amplitude of phase variation induced by decoherer is dependent on the standard deviation of the Normal distribution. The figure 5.19 show that the simulations and the experimental results leads the same results. This correspondence made it possible to accept the model formulated to describe the decoherer.

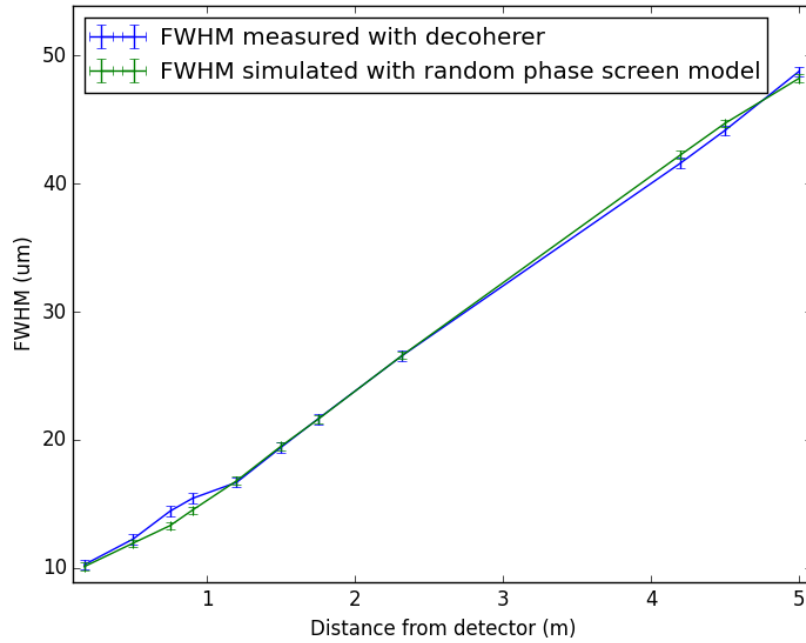


Figure 5.19: FWHM computed for different Normal random phase screen models are compared with the measured FWHM. The compared random phase screens have the same phase amplitude variation ($\sigma = 1$), and different coherence length.

Conclusions

In view of the recent upgrade of ESRF and the growing necessity of simulation software to assess different criticalities of experiments performed in synchrotron facilities, in this thesis project I have presented the formalism of diffraction obtained with a theory that closely resembles the one of linear systems, namely the plane wave decomposition theory. I have developed a scaled Fresnel propagator, based on the theoretical work of J. D. Schmidt, that makes it possible to obtain a zoomed in (or out) image of a propagated wavefront. The strength of the software implementation of the propagator resides in the use of the *FFT* algorithm that makes it possible to solve the diffraction integral, that describes the propagation of a wavefront, much faster (it requires $\sim N^2 \log_2 N$ operations instead of $\sim N^2 \cdot N^2$ to solve the 2D integral). The problems of aliasing and rippling, introduced by the use of the computer algorithm, have been addressed leading to two simple formulas that show the correct range of values for the magnification factor to use in order not to have any artifacts in the images. Such conditions for well sampling the wavefront and the Fresnel propagator, found with theoretical considerations, have been verified against analytical results, against the popular software SRW for the simulation of the beamline ID16A of ESRF and against experimental results of the beamline ID17 of ESRF to determine the effect of a decoherer on the beam.

More studies are necessary to determine the validity conditions for more general cases of wavefronts and to develop a tool that makes the choice of the magnification factor quicker and simpler. This work is a step forward in making WOFRY a valid alternative to the other codes already available; a full compatibility with the package COMSYL will be ensured in order to take into account the partial coherence of the synchrotron light. Together with the implementation of non-ideal optical elements, these upgrades will make it possible to virtually simulate an experiment.

The OASYS Graphical Environment

OASYS (OrAnge SYnchrotron Suite) is an Open Source Graphical Environment developed by Manuel Sanchez del Rio (ESRF) and Luca Rebuffi (ELETTRA) [4]. Its aim is to make virtual experiments possible and easy to do thanks to the integration of different tools that can be used from a user friendly Graphical User Interface. It is developed in Python, that is a popular programming language among the scientific community and it is based on the Orange [27] open source platform for data mining from which the interface has been taken.

Virtual simulations of a beamline consist in modeling the propagation of light starting from the source up to the sample. It is essentially made of three main steps: generation of the radiation emitted by electrons when accelerated by the magnetic field of bending magnets, wigglers or undulators. The modeling of the optical elements such as lens, mirrors or slit aperture and, finally, the propagation of the wavefront from one element to the next one up until the sample.

This sequence of steps can be reproduced with a series of widget all connected by a line that represent the propagation of the wavefront from the source to each optical element. This is the reason why OASYS is so intuitive and powerful. An example of the GUI is presented in figure A.1 where we show a simplified example of ID16A with the source modeled by a spherical wavefront with a superimposed Gaussian intensity profile.

OASYS already integrates the packages SHADOW [5] that uses geometrical optics and SRW [20] that exploits physical optics for simulating the propagation of a wavefield. WOFRY is a new tool that is under development with the objective of complementing external codes such as SRW for the simulation in cases in which the diffraction effects are important. A main result of this thesis work is the implementation of the scaled propagator in the package WOFRY, the graphical interface is visible in figure A.2.

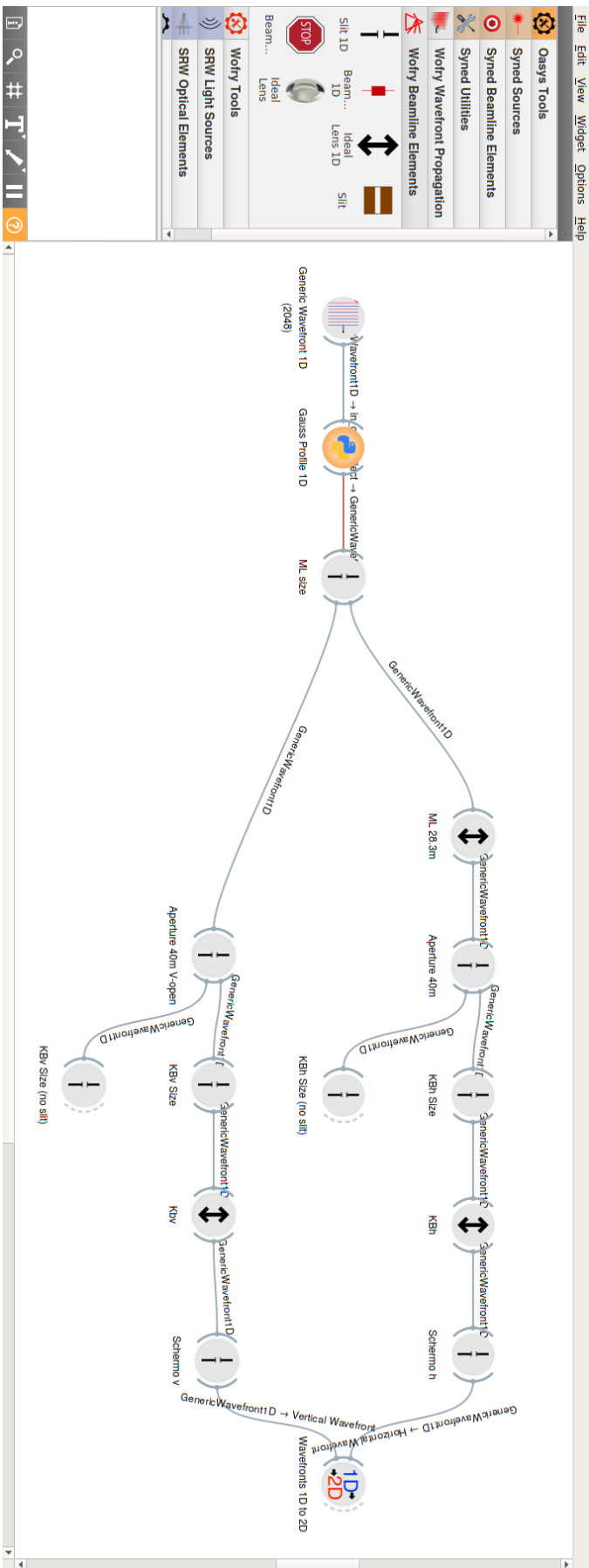


Figure A.1: The figure shows the GUI of OASYS. On the left of the figure there is a menu that let the user choose between the different widgets offered by the various package installed. It is possible to see some of the elements that can now be used in WOFRY. The right part is the white-board where the widget are put and connected. Every widget acts on the input wavefront and the returns the modified output wavefront that is propagated along the lines that connect every widget. The first element from the left generates simple wavefronts (plane, Gaussian and spherical waves), the second element permits to introduce a Python script made by the user. This makes it possible to act with personal functions not yet implemented in WOFRY. The third element represent a slit. At this point the beamline splits in the vertical and horizontal direction to be reunited only at the end where a widget forms a 2D image. This process makes simulations much faster. The element with two arrows represents an ideal lens.

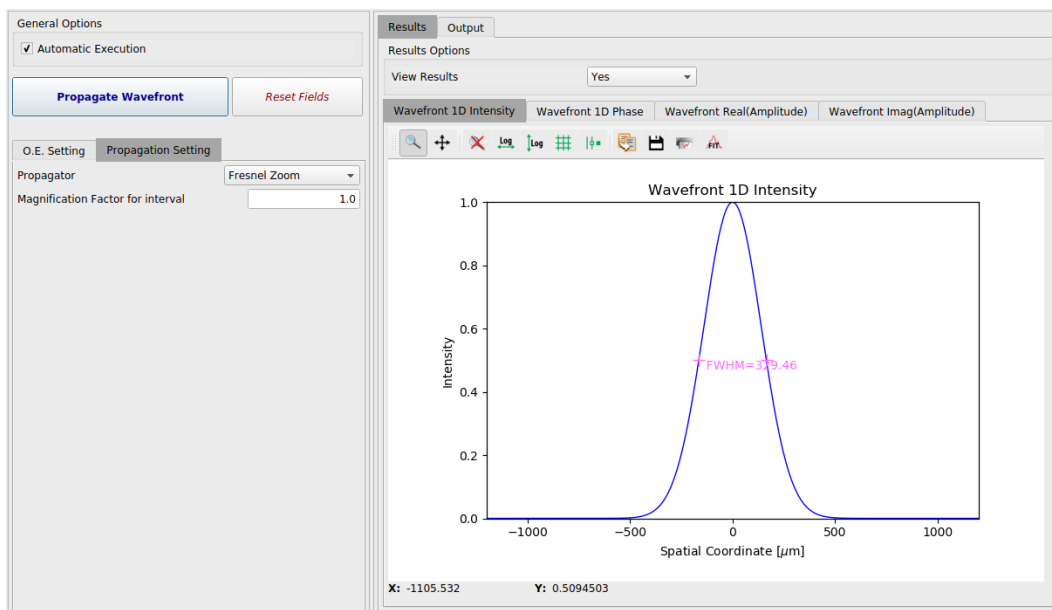
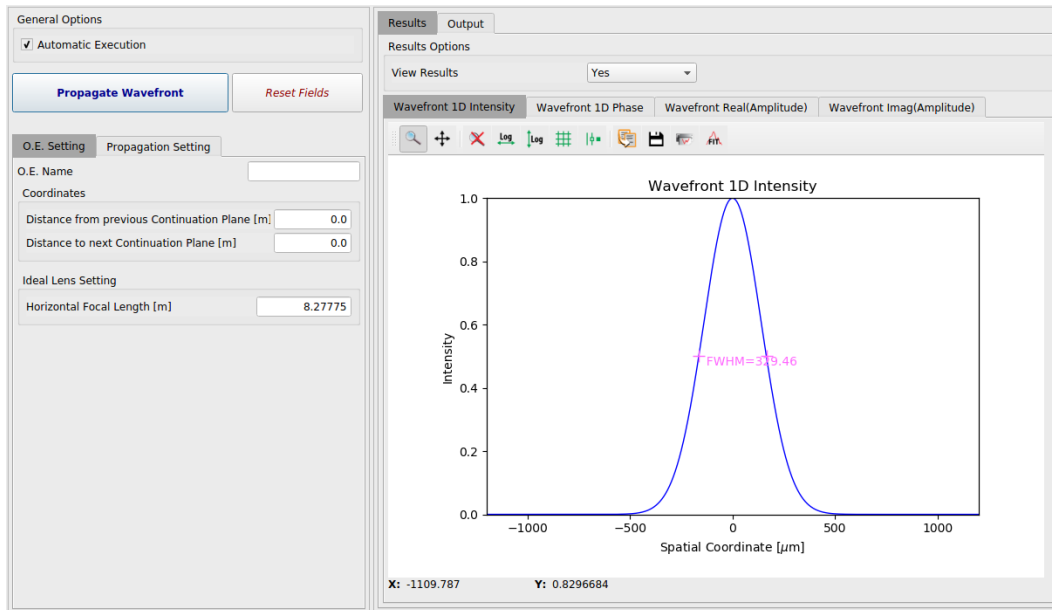


Figure A.2: The two figures show the interface of the lens element. In particular the two views of the command panel on the left. Figure on top shows the propagation distances settings and the focusing factor of the lens. Figure on the bottom shows the panel for the choice of the propagator (scaled Fresnel, the one implemented in this project, Fraunhofer or integral) and the scaling factor. The right part of the figure show the graphical representation of the wavefronts.

Bibliography

- [1] Esrf upgrade programme. <http://www.esrf.eu/about/upgrade>.
- [2] L. Rebuffi and M. Sanchez del Rio. Wofry. <https://github.com/lucarebuffi/wofry>.
- [3] Manuel Sanchez del Rio, Luca Rebuffi, Janez Demsar, Niccolo Canestrari, and Oleg Chubar. A proposal for an open source graphical environment for simulating x-ray optics. *Proc.SPIE*, 9209:9209 – 9209 – 5, 2014.
- [4] L. Rebuffi and M. Sanchez del Rio. Oasys project. <https://github.com/lucarebuffi/wofry>.
- [5] Manuel Sanchez del Rio, Niccolo Canestrari, Fan Jiang, and Franco Cerrina. *SHADOW3*: a new version of the synchrotron X-ray optics modelling package. *Journal of Synchrotron Radiation*, 18(5):708–716, Sep 2011.
- [6] Mark Glass and Manuel Sanchez del Rio. Coherent modes of x-ray beams emitted by undulators in new storage rings. *EPL (Europhysics Letters)*, 119(3):34004, 2017.
- [7] O. Chubar. Srw. <https://github.com/ochubar/SRW>.
- [8] J.W. Goodman. *Introduction to Fourier Optic*. McGraw-Hill, 2nd edition, 1996.
- [9] R.N. Bracewell. *Two-Dimensional Imaging*. Prentice Hall Signal Processing Series. Prentice Hall, 1995.
- [10] Max Born, Emil Wolf, A. B. Bhatia, P. C. Clemmow, D. Gabor, A. R. Stokes, A. M. Taylor, P. A. Wayman, and W. L. Wilcock. *Principles of Optics: Electromagnetic Theory of Propagation, Interference and Diffraction of Light*. Cambridge University Press, 7 edition, 1999.
- [11] Jason D. Schmidt. *Numerical Simulation of Optical Wave Propagation*. SPIE Press, Bellingham, WA, USA, 2010.

- [12] William H. Press, Saul A. Teukolsky, William T. Vetterling, and Brian P. Flannery. *Numerical Recipes 3rd Edition: The Art of Scientific Computing*. Cambridge University Press, New York, NY, USA, 3 edition, 2007.
- [13] E. Oran Brigham. *The Fast Fourier Transform and Its Applications*. Prentice-Hall, Inc., Upper Saddle River, NJ, USA, 1988.
- [14] David Paganin. *Coherent x-ray optics*. Oxford University Press Oxford, New York, 2006.
- [15] George C. Sherman. Application of the convolution theorem to rayleigh’s integral formulas. *J. Opt. Soc. Am.*, 57(4):546–547, Apr 1967.
- [16] Éamon Lalor. Conditions for the validity of the angular spectrum of plane waves*. *J. Opt. Soc. Am.*, 58(9):1235–1237, Sep 1968.
- [17] James W. Cooley and John W. Tukey. An algorithm for the machine calculation of complex fourier series. *Mathematics of Computation*, 19(90):297–301, 1965.
- [18] A. D. Marshall and R. R. Martin. *Computer Vision, Models and Inspection*. World Scientific Publishing Co., Inc., River Edge, NJ, USA, 1992.
- [19] Vincent Favre-Nicolin, Johann Coraux, Marie-Ingrid Richard, and Hubert Renevier. Fast computation of scattering maps of nanostructures using graphical processing units. *Journal of Applied Crystallography*, 44(3):635–640, Jun 2011.
- [20] O. Chubar and P. Elleaume. Accurate and efficient computation of synchrotron radiation in the near field region. *Conf. Proc.*, C980622:1177–1179, 1998. [,1177(1998)].
- [21] L. Rebuffi and M. Sanchez del Rio. Oasys (orange synchrotron suite): an open-source graphical environment for x-ray virtual experiments. *Proc.SPIE*, 10388:10388 – 10388 – 9, 2017.
- [22] Niccolo Canestrari, Oleg Chubar, and Ruben Reininger. Partially coherent x-ray wavefront propagation simulations including grazing-incidence focusing optics. *Journal of Synchrotron Radiation*, 21(5):1110–1121, Sept 2014.

- [23] Caterina Amendola. Implementation of a decoherer system at ID17 of the ESRF. Master's thesis, Politecnico di Milano, School of Industrial and Information Engineering, Department of Physics, Italy, 2018.
- [24] Kaye S. Morgan, Sarah C. Irvine, Yoshio Suzuki, Kentaro Uesugi, Akihisa Takeuchi, David M. Paganin, and Karen K.W. Siu. Measurement of hard x-ray coherence in the presence of a rotating random-phase-screen diffuser. *Optics Communications*, 283(2):216 – 225, 2010.
- [25] S. C. Irvine, K. S. Morgan, Y. Suzuki, K. Uesugi, A. Takeuchi, D. M. Paganin, and K. K. W. Siu. Assessment of the use of a diffuser in propagation-based x-ray phase contrast imaging. *Opt. Express*, 18(13):13478–13491, Jun 2010.
- [26] Alexander Goikhman, Ivan Lyatun, Petr Ershov, Irina Snigireva, Pawel Wojda, Vladimir Gorlevsky, Alexander Semenov, Maksim Sheverdyayev, Viktor Koletskiy, and Anatoly Snigirev. Highly porous nanoberyllium for X-ray beam speckle suppression. *Journal of Synchrotron Radiation*, 22(3):796–800, May 2015.
- [27] Janez Demšar, Tomaž Curk, Aleš Erjavec, Črt Gorup, Tomaž Hočevar, Mitar Milutinovič, Martin Možina, Matija Polajnar, Marko Toplak, Anže Starič, Miha Štajdohar, Lan Umek, Lan Žagar, Jure Žbontar, Marinka Žitnik, and Blaž Zupan. Orange: Data mining toolbox in python. *Journal of Machine Learning Research*, 14:2349–2353, 2013.